4/28/95

SANDIA REPORT

SAND94–3248 • UC–704
Unlimited Release
Printed February 1995

Final Report on LDRD Project: Quantum Confinement and Light Emission in Silicon Nanostructures

T. R. Guilinger, M. J. Kelly, D. M. Follstaedt, D. A. Redman, E. H. Chason, D. R. Tallant, J. C. Barbour, J. S. Custer, A. J. Howard, D. Dimos, S. R. Lee, J. W. Medernach, J. O. Stevenson

Prepared by
Sandia National Laboratories
Albuquerque, New Mexico 87185 and Livermore, California 94550
for the United States Department of Energy
under Contract DE-AC04-94AL85000

Issued by Sandia National Laboratories, operated for the United States Department of Energy by Sandia Corporation.

Available to DOE and DOE contractors from
Office of Scientific and Technical Information
PO Box 62
Oak Ridge, TN 37831

Prices available from (615) 576-8401, FTS 626-8401

Available to the public from
National Technical Information Service
US Department of Commerce
5285 Port Royal Rd
Springfield, VA 22161

NTIS price codes
Printed copy: A04
Microfiche copy: A01

DISCLAIMER

Portions of this document may be illegible in electronic image products. Images are produced from the best available original document.

SAND 94-3248
Unlimited Release
Printed February 1995

Distribution
Category UC-704

Final Report on LDRD Project: Quantum Confinement and Light Emission in Silicon Nanostructures

T. R. Guilinger, 1841, M. J. Kelly, 1824, D. M. Follstaedt, 1112, D. A. Redman, 1112, E. H. Chason, 1112, D. R. Tallant, 1823, J. C. Barbour, 1111, J. S. Custer, 1111, A. J. Howard, 1322, D. Dimos, 1845, S. R. Lee, 1111, J. W. Medernach, 1332, and J. O. Stevenson, 1841

Sandia National Laboratories
Albuquerque, NM 87185

Abstract

Electrochemically formed porous silicon (PS) was reported in 1991 to exhibit visible photoluminescence. This discovery could lead to the use of integrated silicon-based optoelectronic devices. This LDRD addressed two general goals for optical emission from Si: (1) investigate the mechanisms responsible for light emission, and (2) tailor the microstructure and composition of the Si to obtain photoemission suitable for working devices. PS formation, composition, morphology, and microstructure have been under investigation at Sandia for the past ten years for applications in silicon-on-insulator microelectronics, micromachining, and chemical sensors. We used this expertise to form luminescent PS at a variety of wavelengths and have used analytical techniques such as *in situ* Raman and X-ray reflectivity to investigate the luminescence mechanism and quantify the properties of the porous silicon layer. Further, our experience with ion implantation in Si lead to an investigation into alternate methods of producing Si nanostructures that visibly luminesce.

Table of Contents

Final Report on LDRD Project: Quantum Confinement and Light Emission in Silicon Nanostructures

Case Number: 3505.220

Project Manager: S. T. Picraux, 1112

Principal Investigators: T. R. Guilinger, 1841, M. J. Kelly, 1824, D. M. Follstaedt, 1112, D. A. Redman, 1112, E. H. Chason, 1112, D. R. Tallant, 1823, J. C. Barbour, 1111, J. S. Custer, 1111, A. J. Howard, 1322, D. Dimos, 1845, S. R. Lee, 1111, J. W. Medernach, 1332, and J. O. Stevenson, 1841

Abstract

Electrochemically formed porous silicon (PS) was reported in 1991 to exhibit visible photoluminescence. This discovery could lead to the use of integrated silicon-based optoelectronic devices. This LDRD addressed two general goals for optical emission from Si: (1) investigate the mechanisms responsible for light emission, and (2) tailor the microstructure and composition of the Si to obtain photoemission suitable for working devices. PS formation, composition, morphology, and microstructure have been under investigation at Sandia for the past ten years for applications in silicon-on-insulator microelectronics, micromachining, and chemical sensors. We used this expertise to form luminescent PS at a variety of wavelengths and have used analytical techniques such as *in situ* Raman and X-ray reflectivity to investigate the luminescence mechanism and quantify the properties of the porous silicon layer. Further, our experience with ion implantation in Si lead to an investigation into alternate methods of producing Si nanostructures that visibly luminesce.

Accomplishments

Our work both in characterization of luminescence and properties of PS and in the use of He implantation to form novel Si nanostructures led to 9 meeting presentations and 7 refereed publications over the life of this project. The Bibliography below details the presentations and publications. Attached to this SAND report as appendices are copies of the 7 refereed publications resulting from this work. Here, we summarize the important findings from the attached publications. Based on work already completed, we expect to complete one remaining journal publication describing in detail our innovative work using *in situ* Raman spectroscopy to analyze the composition of porous silicon while measuring its photoluminescence.

We used He ion implantation to create a dense layer of nanocavities in silicon. We tailored their size and shape by varying annealing times and temperatures. Hydrogen was introduced in a controlled fashion to produce monohydride termination of the interior surfaces of the nanocavities. A variety of passivation processess were performed, none of which produced visible photoluminescence (PL) from the implanted strucures. We did, however, demonstrate that a 120 nm blue shift in the peak of the PL emission band from porous layers formed on implanted wafers was observed when compared to identically prepared porous layers formed on unimplanted wafers. There was also an obvious difference in microstructure between the layers grown on the implanted and unimplanted substrates as observed by TEM. We ascribed this structure difference to the following model. The He bubble layer forms a fully depleted region extending to the sample surface. This impedes anodic etching until the layer is breached in scattered, localized regions as evidenced by TEM micrographs. Etching of the initially porous bubble layer then proceeds very rapidly laterally as well as vertically. The additional porosity effected by He ion implantation effectively shrinks the crystalline silicon domains between the

nanocavities and leads to the observed blue shift. The observed blue shift thus supports the quantum confinement model for PS photoluminescence.

We used X-ray reflectivity as a non-destructive method for measuring the thickness of porous silicon layers as well as the interfacial roughness between the porous silicon and the single crystal silicon substrate. Thickness and interfacial roughness measured using this method compared favorably with values measured using TEM and atomic force microscopy. Due to X-ray absorption limitations imposed by the PS layer, the maximum thickness of porous silicon that can be examined using X-ray reflectivity was estimated to be about 200 nm depending on the porosity of the layer. Therefore, this technique is limited to the analysis of thin film PS structures.

We also determined the structure of PS films using double-crystal diffractometry combined with position-sensitive X-ray detection to image the reciprocal space structure of the material. The PS material appeared to range in structure from a strained, single-crystal, sponge-like material exhibiting long-range coherency to isolated, dilated nonocrystals embedded in an amorphous matrix. Reciprocal space analysis of n^+ and p^+ porous silicon showed these materials are strained single-crystals with a spatially-correlated array of vertical pores. The vertical pores in these crystals are surrounded by nanoporous or nanocrystalline domains as small as a few nm in size which produce diffuse diffraction indicating their presence.

In other work, Raman and photoluminescence (PL) spectra were obtained both *ex situ* and *in situ* on PS samples that emitted visible light. The results generally showed a correlation of blue-shifted PL with increased oxidation. In one set of *ex situ* experiments, however, we observed an inconsistency in the shift of the wavelength of maximum luminescence intensity for PS samples that exhibited oxygenated character in the Raman spectra. A higher anodization current density produced a red shift in the PL spectra in one experiment, while chemical dissolution of the PS by hydrofluoric acid (HF) produced the well-known blue shift. In two *in situ* experiments, we observed very weak and red-shifted PL for a PS sample immersed in HF (compared to the same sample measured later in air) while in another we immersed air-exposed PS in water and observed a 15-fold increase in PL intensity along with a blue shift in the luminescence maximum.

Finally, we developed a method for the reduction of the PL signal from PS by ion-irradiation. Ion irradiation with 250 keV Ne was used to controllably reduce the integrated PL signal by 20% after a fluence of $4x10^{12}$ Ne cm^{-2} and completely eliminate the PL signal after a fluence of $4x10^{13}$ Ne cm^{-2}. We used vacuum and air annealing to recover ion-induced damage but the high temperatures for annealing caused elimination of the PL signal.

Bibliography

Publications

1. Redman, D. A., D. M. Follstaedt, T. R. Guilinger, and M. J. Kelly. 1994. "Photoluminescence and Passivation of Silicon Nanostructures", *Appl. Phys. Lett. 65*, 2386.

2. Guilinger, T. R., M. J. Kelly, E. H. Chason, T. J. Headley, and A. J. Howard, "Non-Destructive Measurement Of Porous Silicon Thickness Using X-Ray Reflectivity", Submitted to *J. Electrochem. Soc.*

3. Chason, E. H., T. R. Guilinger, M. J. Kelly, T. J. Headley, and A. J. Howard. 1995. "Non-Destructive Characterization of Porous Silicon Using X-Ray Reflectivity", Proceeedings of the Materials Research Society, to be published.

4. S. R. Lee, J. C. Barbour, J. W. Medernach, J. O. Stevenson, and J. S. Custer. 1995. "Reciprocal Space Analysis of the Microstructure of Luminescent and Non-Luminescent Porous Silicon Films", Proceeedings of the Materials Research Society, to be published.

5. Kelly, M. J., T. R. Guilinger, D. R. Tallant, D. A. Redman, and D. M. Follstaedt. 1993. "Visible Light Emission from Porous Silicon Examined by Photoluminescence and Raman Spectroscopy", Proceedings of the Materials Research Society, 283, 115.

6. Redman, D. A., D. M. Follstaedt, T. R. Guilinger, and M. J. Kelly. 1993. "Photoluminescence of Silicon Nanostructures Formed by Ion Implantation", Proceedings of the Materials Research Society, 279, 201.

7. Barbour, J. C., D. Dimos, T. R. Guilinger, and M. J. Kelly. 1992. "Control of Photoluminescence from Porous Silicon", *Nanotechnology 3,* 202.

Presentations

1. Chason, E. H., T. R. Guilinger, M. J. Kelly, T. J. Headley, and A. J. Howard. 1994. "Non-Desctructive Characterization of Porous Silicon Using X-Ray Reflectivity", MRS Fall Meeting, Boston, MA, Nov. 28-Dec. 2.

2. S. R. Lee, J. C. Barbour, J. W. Medernach, J. O. Stevenson, and J. S. Custer. 1994. "Reciprocal Space Analysis of the Microstructure of Luminescent and Non-Luminescent Porous Silicon Films",MRS Fall Meeting, Boston, MA, Nov. 28-Dec. 2.

3. Guilinger, T. R., M. J. Kelly, D. A. Redman, D. M. Follstaedt, and D. R. Tallant. 1993. "Visible Light Emission from Silicon Nanostructures", Technology Transfer Opportunities with the National Labs, Albuquerque, NM, Oct. 25, 1993.

4. Guilinger, T. R., M. J. Kelly, D. A. Redman, D. R. Tallant, J. C. Barbour, E. H. Chason, and D. M. Follstaedt. 1993. "Mechanistic Studies of Visible Photoluminescence from Silicon Nanostructures", 18th DOE Surface Studies Conference, Santa Fe, NM, April 27-30.

5. Redman, D. A., D. M. Follstaedt, T. R. Guilinger, and M. J. Kelly. 1992. "Photoluminescence of Silicon Nanostructures Formed by Ion Implantation", MRS Fall Meeting, Boston, MA, Nov. 30-Dec. 4.

6. Kelly, M. J., T. R. Guilinger, D. A. Redman, D. R. Tallant, and D. M. Follstaedt. 1992. "Visible Light Emission from Porous Silicon Examined by Photoluminescence and Raman Spectroscopy", MRS Fall Meeting, Boston, MA, Nov. 30-Dec. 4.

7. Guilinger, T. R., M. J. Kelly, D. A. Redman, D. M. Follstaedt, and D. R. Tallant. 1992. "Visible Light Emission from Porous Silicon Nanostructures Formed by Anodization and Ion Implantation", New Mexico ACers/MRS Meeting, Santa Fe, NM, Oct. 23.

8. Barbour, J. C., D. B. Dimos, T. R. Guilinger, and M. J. Kelly. 1992. "Control of Photoluminescence from Porous Silicon", Workshop on Atoms and Clusters 1992, Atami, Shizuoka, Japan, Jan. 8-10.

9. Barbour, J. C., D. B. Dimos, T. R. Guilinger, M. J. Kelly, and S. S. Tsao. 1991. "Ion-Irradiation Effects on Photoluminescence from Porous Silicon", MRS Fall Meeting, Boston, MA, Dec. 2-6.

Appendix I. "Photoluminescence and Passivation of Silicon Nanostructures"

Photoluminescence and passivation of silicon nanostructures

D. A. Redman, D. M. Follstaedt, T. R. Guilinger, and M. J. Kelly

Sandia National Laboratories, Albuquerque, NM 87185-1056.

Abstract

A new method was used to fabricate nanometer-scale structures in Si for photoluminescence studies. Helium ions were implanted to form a dense subsurface layer of small cavities (1-16 nm diameter). Implanted specimens subjected to annealing in a variety of atmospheres yielded no detectable photoluminescence. However, implantation combined with electrochemical anodization produced a substantial blue shift relative to anodization alone. This blue shift is consistent with the quantum confinement model of photoluminescence in porous silicon.

Reports of light emission from electrochemically etched porous silicon[1] (PS) have suggested the possibility of silicon-based optoelectronic devices compatible with current VLSI processing technology. Recent work indicates that an explanation of the luminescence must involve both the modified electronic states in the silicon microstructures and the interaction of these states with the surface. For example, an "undulating wire" model proposed to explain structure in the low temperature near-resonant PL excitation spectra[2] does not fully explain the reversible shifts in the PL band observed in titration experiments.[3] Theoretical approaches have concentrated on the modifications to the silicon bulk electron states effected by the reduced dimensionality of the PS,[4] however, the shape of the potential imposed by the boundary of the microstructure depends on the nature of the chemical bond between the surface silicon atoms and the chemisorbed species.

The wet chemical methods for producing PS involve an aqueous HF electrolyte and necessarily expose the porous material to fluorine, hydrogen, and oxygen. Furthermore, a native oxide and some hydrocarbon contamination covers the exposed surfaces when the specimen is removed from the electrolyte and exposed to air.[5] The simultaneous presence of all the elements required for both quantum confinement and surface state models precludes independent evaluation of either. In the hope of elucidating the relative contribution of each model to the luminescence mechanism, we formed nanometer-size structures ("nanostructures") in silicon using helium ion implantation to produce a dense, subsurface layer of bubbles.[6,7] This porous layer is free from contamination and is removed from any oxidizing ambient, making the process compatible with contamination-free VLSI processing techniques. Furthermore, the interior surfaces can be passivated in a relatively controlled fashion as compared to wet chemical methods. The nanostructure dimensions are similar to the pore diameters observed in electrochemically produced PS. We find that the bubble layer has a dramatic effect on the formation and luminescence properties of PS even though nanostructures formed by implantation alone do not luminesce.

Helium-implanted (100) Si samples were prepared using 30 keV He^+ at room temperature. Annealing at 600-800 °C was carried out in vacuum or in atmospheres of hydrogen or deuterium for times up to 88 hours. Details of the specimen preparation are provided elsewhere.[8] Figure 1a shows a cross-section transmission electron micrograph (TEM) of a specimen implanted with $1.0x10^{17}$ He/cm^2. The specimen contains helium bubbles of 1-2 nm diameter along with substantial implantation damage. Annealing for 10 hours at 800 °C in vacuum removes some of the implantation damage, allows the helium to diffuse out of the specimen, and coarsens the voids to an average size of 16 nm. A well-defined cavity layer exists at depths between 0.15 - 0.35 μm after annealing.

Porous silicon was prepared using 0.5 - 1.2 Ω-cm (100), *p*-type silicon wafers. These were anodized in a 2-electrode electrochemical cell, with electrical contact to the backside of the silicon sample made by pressing a gold disk against it. A 5% HF solution at a current density of 0.55 mA/cm^2 produced a layer approximately 73% porous with a thickness determined by the reaction time. After anodization, the wafers were rinsed in water and allowed to air dry. Processed wafers were stored in air.

Photoluminescence (PL) measurements were made at room temperature for both as-implanted and implanted/annealed specimens, both before and after H_2 soaking. Spectra were taken using a 0.22 m double monochromator (SPEX 1680B) employing 1200 gr/mm gratings blazed at 500 nm. Slit widths were typically 100 - 500 μm. A cooled GaAs photocathode photomultiplier tube was used in both a synchronous (lock-in) detection mode and a photon counting mode with a root mean square dark noise of less than one count. An argon laser operating at 457 nm was used for excitation at power densities less than 10 W/cm^2.

Figure 2 compares a typical photoluminescence spectrum from an implanted specimen to that from electrochemically prepared PS on a 1 Ω-cm (100), *p*-type wafer. The electrochemically produced specimen was 73% porous, as determined by gravimetric measurements on full wafers processed under identical conditions. The implanted specimen received $1.0x10^{17}$ He/cm^2 at 30 keV with no post-implant annealing prior to D_2 soaking at 600°C for 67 hours. The

electrochemically-prepared specimen yields a strong PL band extending from 550 nm to 825 nm and centered at 694 nm (spectrum a). The implanted specimen shows no evidence of photoluminescence over a similar band (spectrum b). Transmission through 0.35 μm of silicon is ~ 93% at 700 nm; thus absorption in the silicon overlayer is not a significant factor in detecting light emitted from the implant region.

The lack of photoluminescence from the implanted specimen can be explained in terms of both the microstructure and the effects of internal surfaces. Efficient optical emission requires enhanced radiative recombination (direct band-to-band or excitonic) and simultaneous suppression of nonradiative recombination. Theory suggests that the zone center matrix element for direct optical recombination becomes significant in silicon only when the crystalline dimensions are reduced to < ~10 nm.[4] The 600 °C anneal is expected to coarsen the cavities to ~8 nm in diameter, but crystalline regions between them would be greater than 10 nm. Furthermore, the porosity is relatively low compared with that of PS. The He cavity layer of implanted specimens has a porosity of ~7%, whereas PS can have porosities greater than 90%. High connectivity of the crystalline regions between cavities presents a correspondingly small potential barrier for carrier diffusion into the substrate. This apparently inhibits radiative recombination by precluding the formation of stable excitons or localized excess carriers within the implanted layer.

Implantation creates additional pathways for nonradiative recombination that are not found in PS with comparable microcrystallite sizes; hence complete passivation is critical. The importance of passivating surface states for luminescence in PS is well known.[9] The as-implanted specimen shown in Fig. 1(a) has nanostructures with appropriate dimensions for quantum shifts in the silicon band structure, however dislocations from implantation damage permeate the layer. This damage provides nonradiative recombination centers in addition to the surface states arising from dangling bonds on the internal surfaces of the voids.[10] Annealing removes some of the dislocations at the expense of reduced carrier confinement. We attempted to passivate defects and dangling bonds by soaking the samples in D_2 or H_2 at 600 °C. Examination of treated specimens with FTIR shows that monohydride (Si-H) bonds preferentially form on the cavity interiors.[11]

These and other means of passivation, including ECR plasma hydrogenation and HF immersion, were not successful in producing photoluminescence, even when amounts of D expected to saturate all dangling bonds were found to be present with ion-beam analysis.[12] Higher He fluences, up to 4.2×10^{17} He/cm^2, were also used in the hope of achieving greater porosity and carrier confinement, but photoluminescence was not observed.[8]

We have also examined the photoluminescence of PS formed on a He-implanted substrate. The wafer was implanted with 1×10^{17} He/cm^2 and was subsequently anodized over 15% of its area. A reaction time of 656 seconds under the anodization conditions described above produced a 73% porous layer with a depth of 0.3 μm in an unimplanted wafer. It was thus expected that identical anodization of the implanted substrate would produce a porous region extending into the layer with nanometer-sized bubbles, and that the layer would affect the PS etch rate and final porosity. Figure 2 shows PL spectra from this specimen. Spectrum (b) was recorded with the excitation incident on the implanted and D_2-soaked substrate alone. Spectrum (c) shows the spectrum recorded under identical conditions with the excitation incident on the porous, implanted surface region. The dominant features of spectrum (c) are the PL band peaking at 590 nm on top of an exponential tail sloping away from the excitation line at 457 nm. The presence of this tail indicates that the anodization enhances the surface scatter of the excitation light to a level that is not rejected by the spectrometer. It has been reported that increasing the porosity of electrochemically produced PS (for a given substrate resistivity) shifts the peak of the PL band to shorter wavelengths.[1] When the exponential tail is subtracted off spectrum (c), there is a 103 nm blue shift of the PL peak from that of the 73% porous specimen in spectrum (a). This blue shift is consistent with a local porosity that is very high in the porous, implanted region. The efficiency of the PL from the anodized, implanted specimen is poor compared to that from the unimplanted porous specimen, perhaps due to implantation damage not present in the virgin wafers.

Figure 1 compares the microstructure of an implanted substrate, an implanted substrate after electrochemical formation of PS, and a thin PS layer on an unimplanted substrate. Figure 1b shows the presence of a surface layer of relatively unaffected crystalline silicon above a layer of

material with graded porosity. At the depth of the cavity layer (0.15-0.35μm) the porous Si shows a "texture" parallel to the surface, apparently due to lateral propagation of the anodization. A finer structure is seen near the substrate side of the layer. Furthermore, the bubbles formed by He implantation alone (Fig. 1a) are confined to depths less than 0.35 μm, while the porous layer in Fig. 1b extends to a depth of 0.45 μm and forms an abrupt interface with the substrate. Figure 1c shows the structure resulting from identical anodization (except for a shortened reaction time of 188 seconds) of an unimplanted wafer. In this case the fine "texture" appears to run normal to the surface and is uniform throughout the layer.

We ascribe the structure and PL spectrum of the implanted and anodized specimen to the following model. The He bubble surfaces have ambipolar dangling bonds that trap carriers.[10] This charges the layer and causes bending of the carrier bands. To conduct charge to the anodizing surface, the carriers must overcome the electrostatic barrier presented by the layer. Moreover, a fully depleted carrier region is expected to extend to the sample surface. These features impede anodic etching until the overlayer is breached in scattered, localized regions. Figure 3 shows a lower magnification cross-section TEM image typical of such regions, which were found to be separated by ~3 μm. Etching of the initially porous bubble layer then proceeds both laterally and vertically. The initial porosity and charge transport properties of the nanocavity layer enhance the lateral etch rate by ~10x, allowing connection of the subsurface region between the breach points. We believe the additional porosity of the nanocavity layer effectively shrinks the crystalline silicon domains produced by anodization and leads to increased quantum confinement and the observed blue shift.

In conclusion, we used He ion implantation to create a porous layer of nanocavities in silicon. We tailored the size and number of the cavities by varying He fluence and annealing temperature. A variety of passivation processes were used to introduce hydrogen in a controlled fashion, but none produced visible photoluminescence from the implanted structures. However, we have demonstrated a 103 nm blue shift in the peak of the PL emission band from porous layers formed

on implanted wafers when compared to identically prepared porous layers formed on unimplanted wafers.

The authors thank M. P. Moran for preparing cross-section TEM specimens and D. M. Bishop for performing the ion implantations and the anneals. Discussions with J. C. Barbour, S. M. Myers, W. R. Wampler and H. J. Stein were quite valuable. This work performed at Sandia National Laboratories is supported by the U. S. Department of Energy under contract DE-AC04-94AL85000.

References

1. L. T. Canham, Appl. Phys. Lett. **57**, 1046 (1990).

2. P. D. J. Calcott, K. J. Nash, L. T. Canham, M. J. Kane, and D. Brumhead, Mat. Res. Soc. Symp. Proc. **283**, 143 (1993).

3. K.-H. Li, C. Tsai, J. Sarathy, and J. C. Campbell, Appl. Phys. Lett. **62** (24), 3192 (1993).

4. A. J. Read, R. J. Needs, K. J. Nash, L. T. Canham, P. D. J. Calcott, and A. Qteish, Phys. Rev. Lett., **69** (8), 1232 (1992).

5. L. T. Canham, M. R. Houlton, W. Y. Leong, C. Pickering, and M. J. Keen, J. Appl. Phys., **70**, 422 (1991).

6. A. Van Veen, C. C. Griffioen, and J. H. Evans, Mat. Res. Soc. Symp. Proc. **107**, 449 (1988); C. C. Griffioen, J. H. Evans, P. C. DeJong, and A. Van Veen, Nucl. Inst. Meth. **B27**, 417 (1987).

7. D. M. Follstaedt, S. M. Myers, and H. J. Stein, Mat. Res. Soc. Symp. Proc. **279** (1993).

8. D. A. Redman, D. M. Follstaedt, T. Guilinger, and M. Kelly, Mat. Res. Soc. Symp. Proc. **279**, 201 (1993).

9. B. K. Meyer, V. Petrova-Koch, T. Muschik, H. Linke, P. Omling, and V. Lehmann, Appl. Phys. Lett. **63** (14), 1930 (1993).

10. C. H. Seager, S. M. Myers, R. A. Anderson, W. L. Warren, and D. M. Follstaedt, Phys. Rev. -B, in press.

11. W. R. Wampler, S. M. Myers, and D. M. Follstaedt, Phys. Rev. B **48**, 4492 (1993).

12. D. M. Bishop, W. R. Wampler, and J. C. Barbour, private communication, 1993.

Figure Captions

FIG. 1. (a) [110] cross-section TEM bright-field image of (001) Si implanted with 1.0×10^{17} He/cm^2 at 30 keV. (b) Similar image after anodic etching in 5% HF solution at a current density of 0.55 mA/cm^2 for 656 seconds. (c) Image of a porous layer produced by similar anodic etching of an unimplanted substrate for 188 seconds. Under-focus TEM conditions were chosen to obtain the best feature contrast.

FIG. 2. (a) PL spectrum obtained from a 73% PS wafer with no implant normalized to scale of curves b and c. Structure in the spectrum at 685 nm is a spectrometer artifact. (b) Spectrum obtained from a He implanted and deuterium passivated wafer similar to that shown in Fig 1a. The solid line is a least square exponential fit to the raw data. (c) Spectrum obtained from porous region of the same implanted wafer as described in the text. The solid line is a smoothed representation the raw data intended as guide for the eye.

FIG. 3. Lower magnification cross-section TEM image of the same specimen shown in Fig. 1b. An area showing etching through the relatively defect free Si overlayer is seen near the center.

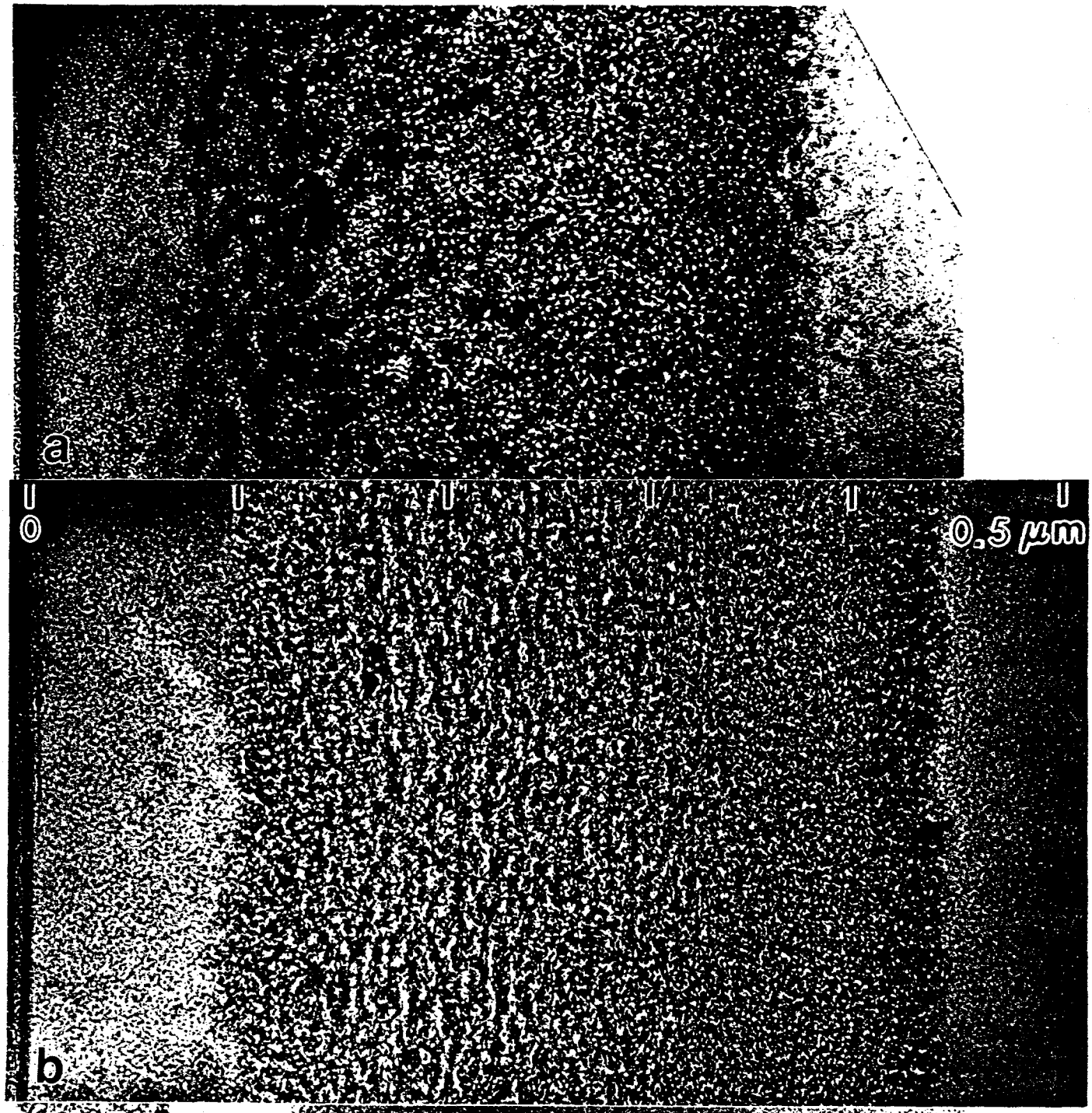
a
0
0.5 µm
b
c

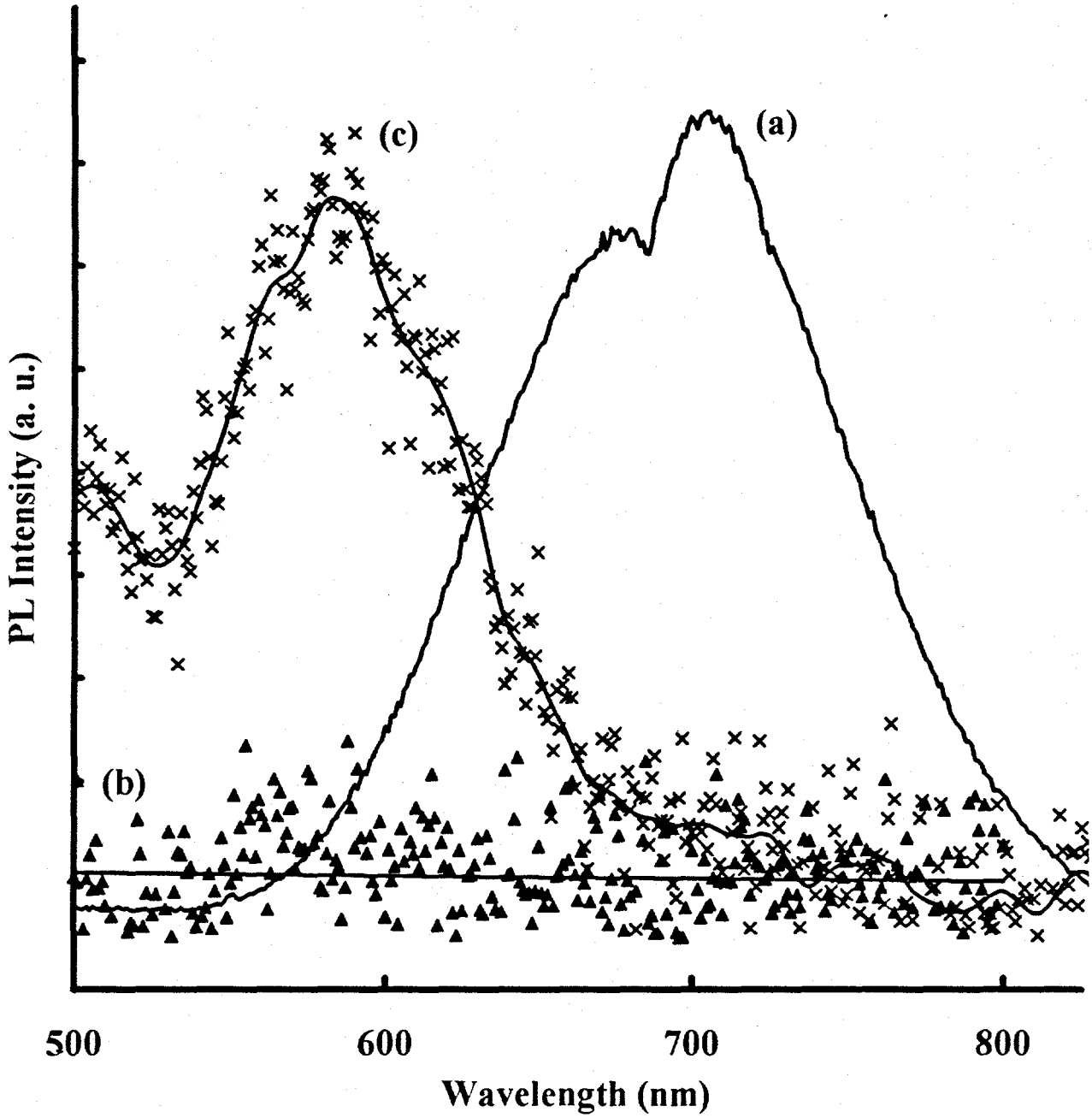
(a)
(b)
(c)
PL Intensity (a. u.)
500
600
700
800
Wavelength (nm)

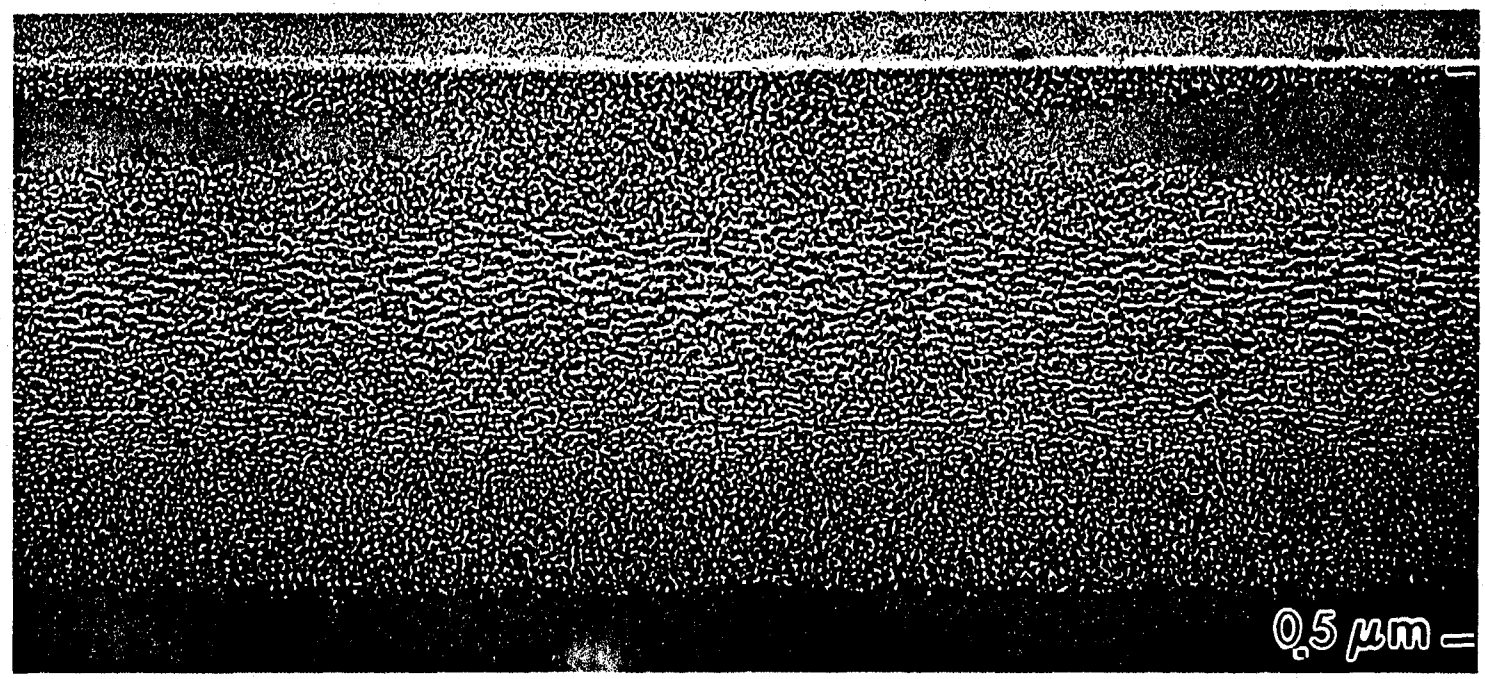
0.5 μm

Appendix II. "Non-Destructive Measurement of Porous Silicon Thickness Using X-Ray Reflectivity"

August 31, 1994 Draft for the Journal of the Electrochemical Society

NON-DESTRUCTIVE MEASUREMENT OF POROUS SILICON THICKNESS USING X-RAY REFLECTIVITY

T. R. Guilinger*, M. J. Kelly* , E. H. Chason, T. J. Headley, and A. J. Howard*
Sandia National Laboratories, Albuquerque, NM 87185

ABSTRACT

In this paper, we describe a non-destructive method based on X-ray reflectivity for measuring the thickness of porous silicon layers as well as the interfacial roughness between the porous silicon and the single crystal silicon substrate. Thickness and interfacial roughness measured using this method compare favorably with values measured using transmission electron microscopy (TEM) and atomic force microscopy (AFM) but differ from values obtained by gravimetric techniques for porous silicon layers thinner than 150 nm.

*Electrochemical Society Active Member

August 31, 1994 Draft for the Journal of the Electrochemical Society

NON-DESTRUCTIVE MEASUREMENT OF POROUS SILICON THICKNESS USING X-RAY REFLECTIVITY

T. R. Guilinger*, M. J. Kelly* , E. H. Chason, T. J. Headley, and A. J. Howard*
Sandia National Laboratories, Albuquerque, NM 87185

ABSTRACT

In this paper, we describe a non-destructive method based on X-ray reflectivity for measuring the thickness of porous silicon layers as well as the interfacial roughness between the porous silicon and the single crystal silicon substrate. Thickness and interfacial roughness measured using this method compare favorably with values measured using transmission electron microscopy (TEM) and atomic force microscopy (AFM) but differ from values obtained by gravimetric techniques for porous silicon layers thinner than 150 nm.

INTRODUCTION

Although the property of visible photoluminescence from porous silicon (then called silicon stain film) was discovered more than 30 years ago [1], renewed interest due to the work of Canham [2] has resulted in numerous publications related to the composition and morphology of porous silicon (PS) and their relation to the mechanism of PS photoluminescence. As yet, no clear model for PS photoluminescence has been accepted although proposed mechanisms include: (1) quantum size effects due to the small size of the PS nanostructures causing band structure modification of the silicon [2,3]; (2) chemiluminescence from Si-O-H polymeric compounds such as siloxene, $Si_6O_3H_6$, and fluorinated derivatives [4]; (3) photoluminescence due to the presence of SiH_x compounds, particularly SiH_2 and SiH_3 [5]; and (4) light emission from hydrogen-terminated amorphous silicon structures [6].

*Electrochemical Society Active Member

In this paper, we describe the use of X-ray reflectivity in the measurement of physical properties of thin PS layers. Analytical tools previously applied to the measurement of the chemical and physical properties of porous silicon layers include the following: X-ray photoelectron spectroscopy (XPS) to examine the chemical species present in porous silicon and associate these chemical species with the PS photoluminescence [6], soft x-ray absorption to measure the differences in absorption spectra between porous and crystalline silicon [7], electron paramagnetic resonance to probe the localization of charge carriers in PS nanostructures [8], small-angle X-ray scattering to determine PS porosity and thickness [9], X-ray fluorescence and diffraction to obtain mean pore size, correlation between pores positions, and local lattice distortions [10], Fourier transform infrared spectroscopy (FTIR) measurements to determine the extent of hydrogen bonding of PS samples [5,11], and Raman spectroscopy to examine the broadening of the crystalline silicon peak to measure the presence of silicon microcrystallites in the 2-3 nm range [12,13,14].

The physical properties of the porous silicon layer, such as porosity and thickness, can be measured in a number of ways including gravimetry [15,16], interferometry [17], and cross-sectional microscopy. Gravimetry and microscopy require destruction of the PS sample. Interferometry, using either infrared or visible light, results in two unknowns in the data analysis: porosity and thickness. For this technique, either an independent measure of porosity or thickness must be made or the interferometry must be performed at multiple angles of incidence. X-ray reflectivity suffers from neither of these problems.

X-ray reflectivity has been used to study the structure of surfaces and interfaces in a large variety of materials. This technique has become popular not only because it is non-destructive but also because X-rays are highly penetrating which makes it possible to study buried interfaces and perform *in situ* studies where non-optical probes cannot be used [18]. The development of a new approach to X-ray reflectivity measurements using energy dispersive detection has made this technique more accessible to laboratory-based X-ray generators [19]. In this approach, the reflectivity is determined as a function of energy at a fixed angle. Working at a fixed angle lessens the experimental difficulty of scanning small angles at high precision.

It is our intent in this paper to show that X-ray reflectivity can be used to accurately determine the thickness and interfacial roughness of porous silicon layers. We will compare the values of thickness and roughness measured by X-ray reflectivity with those determined by cross-section transmission electron microscopy (XTEM), atomic force microscopy (AFM), and gravimetric techniques.

EXPERIMENTAL

Porous silicon was formed by electrochemical anodization of 0.5-1.0 Ω-cm, boron doped, (100) p-Si in a dual-tank electrochemical cell. Details of the design and testing of this cell are given elsewhere [20,21]. The PS samples examined in this paper were formed in 5 wt% HF at 0.58 mA/cm^2 for times ranging from 141 to 376 sec. The total area of PS formed was 45.8 cm^2. Gravimetric measurements, utilizing the weight loss of the silicon sample on anodization and after removal of the PS layer with 7 M NaOH, indicated that these formation conditions produced PS layers about 70-79% porous with thicknesses ranging from 110 to 200 nm.

X-ray reflectivity was performed on samples of porous silicon by exciting the PS in a broad band X-ray source produced from a Mo target on a rotating anode generator operating at 4 kW (40 kV and 100 mA). The X-ray filament was in the line focus mode creating an effective source size of 0.05 cm x 1 cm. The total area of PS sample excited was 5 x 5 mm. The reflectivity was obtained experimentally by measuring the reflected intensity as a function of the scattering vector. In conventional reflectivity measurements, the X-ray energy is kept constant and the scattering vector is scanned by changing the scattering angle. In the energy-dispersive technique, the scattering vector is scanned by fixing the scattering angle (at 1 degree) and measuring the reflected intensity as a function of energy.

The measured reflectivity was analyzed with an optical single layer or multilayer model (Parratt [22]) using a nonlinear least-squares fitting routine to optimize the parameters. The parameters to be varied were the number of

layers, the density and thickness of each layer, and the roughness of the top surface and buried interfaces.

AFM micrographs were taken using a Digital Instruments Nanoscope III atomic force microscope operating in air in contact mode. No sample preparation was required for this non-destructive technique. The AFM has built-in capabilities for the analysis of RMS surface roughness. Images were taken from several areas of each sample with varying sample sizes to yield average RMS roughness over the entire sample.

RESULTS AND DISCUSSION

We prepared four porous silicon samples according to the recipe described above. The samples were prepared under identical conditions with anodization times of 141, 188, 282, and 376 sec providing PS layers with different thicknesses. After determining their X-ray reflectivity, three of the PS samples were cross-sectioned, electrochemically thinned, and then ion-milled for TEM. The reflectivity data was fit to both single layer and multi-layer models. Satisfactory fit of the data to a single layer model was found for all four PS samples. Furthermore, TEM detected only one layer in the samples examined.

Figure 1 shows the X-ray reflectivity data and the single layer fit of the data for the PS sample anodized for 188 sec. The X-ray reflectivity data for each PS sample was analyzed to obtain the thickness, porosity, and roughness of the PS layer. Figure 2 shows the thickness of the porous silicon layers as determined by X-ray reflectivity. Error bars on the X-ray reflectivity data in Figure 2 are at 5% of the measured value representing a conservative estimate of the error associated with the single layer least squares fit of the data by perturbation analysis. A satisfactory linear fit to the thickness data from X-ray reflectivity can be made. This linear fit yields a non-zero x-intercept at about 48 sec suggesting an induction time for the production of porous silicon. If electropolishing were occuring during the first 48 sec, about 8 nm of silicon would be removed before PS formation began (assuming that the number of electrons transferred during electropolishing is 4 per silicon atom removed). We

are currently analyzing PS layers made at anodization times between 0 and 142 sec to determine the validity of the induction time concept.

We used cross-sectional TEM as an independent means to determine the thickness and roughness of three of the PS layers. After digitizing the TEM micrographs, we calculated both the average PS layer thickness over the area of the micrograph (micrographs covered a cross-sectional distance of about 500 nm) and the root mean square roughness of both the PS/silicon interface and the PS surface. Figure 3 shows a portion of a representative XTEM for the PS sample anodized for 188 sec. Thicknesses of the PS layers as calculated from the TEM micrographs are shown in Figure 2. For the PS samples anodized at 141 and 188 sec, thicknesses measured by X-ray reflectivity and XTEM are within 10% of one another and the differences in the measured values are well within the error estimates of the two techniques. For the PS sample anodized for 282 sec, error between the two methods is about 30% although the very large uncertainty in the XTEM measurement, caused by the roughness at the PS/silicon interface, indicates that the difference in thickness determined by the two techniques is nearly within the error estimates for the XTEM.

We routinely determine the thickness and porosity of PS samples by gravimetry. Gravimetric determinations of the porosity and thickness of the porous silicon samples described here showed that porosity varied between 70 and 79% while thicknesses calculated by material balance were 120 nm, 110 nm, 160 nm, and 200 nm for the 141 sec, 188 sec, 282 sec, and 376 sec PS samples, respectively. As shown by the data in Figure 2, thicknesses calculated by gravimetry are consistently higher than those determined by X-ray reflectivity. It should be noted that gravimetric thicknesses are averaged over the entire area of the PS layer (45.8 cm^2) while a 5 x 5 mm area was examined by X-ray reflectivity. Furthermore, for these thin PS layers, considerable error is introduced in gravimetric measurements due to the difficulty in accurately and precisely measuring small (0.01 mg) weight changes on large (10 g) substrates. As shown in Figure 2, the deviation between gravimetric and x-ray reflectivity measurements of thickness decreases with increasing PS layer thickness showing that for larger silicon weight losses, these two methods are in closer agreement.

Figure 4 shows root mean square roughness of the interface between the PS layer and the silicon substrate and of the PS top surface determined by X-ray reflectivity, atomic force microscopy (AFM), and XTEM. The interfacial roughness for AFM was determined by removing the PS layer in 7 M NaOH before AFM analysis. All three analysis methods show that the interfacial roughness of PS is about 5-10 times that of the top PS surface. Further, all three methods are in approximate agreement on the absolute value of the interfacial (about 2-5 nm) and surface (about 0.5 nm) roughness of PS. The AFM measurement of roughness at the PS/substrate interface is probably low due to the smoothing effect of 7M NaOH used to remove the PS layer before AFM analysis. Figure 4 also shows that PS surface roughness is constant with increasing anodization time (this surface roughness is equivalent to that determined by AFM for a virgin silicon wafer) while PS/silicon interfacial roughness increases with increasing anodization time.

CONCLUSIONS

We used X-ray reflectivity as a non-destructive method for measuring the thickness of porous silicon layers as well as the interfacial roughness between the porous silicon and the single crystal silicon substrate. Thickness and interfacial roughness measured using this method compare favorably with values measured using TEM and atomic force microscopy. Due to X-ray absorption limitations imposed by the PS layer, the maximum thickness of porous silicon that can be examined using X-ray reflectivity is estimated to be about 200 nm depending on the porosity of the layer. Therefore, this technique is limited to the analysis of thin film PS structures.

ACKNOWLEDGMENTS

The authors gratefully acknowledge the assistance of Tom Tribble for TEM sample preparation. This work was performed at Sandia National Laboratories supported by the U. S. Department of Energy under contract DE-AC04-94AL85000.

REFERENCES

1. A. Gee, *J. Electrochem. Soc.*, **107**, 787 , (1960).

2. L. T. Canham, *Appl. Phys. Lett.*, **57**, 1046, (1990).

3. A. G. Cullis and L. T. Canham, *Nature*, **353**, 335, (1991).

4. M. S. Brandt, H. D. Fuchs, M. Stutzmann, J. Weber, and M. Cardona, *Solid State Commun.*, **81**, 307, (1992).

5. C. Tsai, K.-H. Li, D. S. Kinosky, R.-Z. Qian, T.-C. Hsu, J. T. Irby, S. K. Banerjee, A. F. Tasch, J. C. Campbell, B. K. Hance, and J. M. White, *Appl. Phys. Lett.*, **60**, 1700, (1992).

6. R. P. Vasquez, R. W. Fathauer, T. George, A. Ksendzov, and T. L. Lin, *Appl. Phys. Lett.*, **60**, 1004, (1992).

7. T. van Buuren, Y. Gao, T. Tiedje, J. R. Dahn, and B. M. Way, *Appl. Phys. Lett.*, **60**, 3013, (1992).

8. S. V. Bhat, K. Jayaram, D. V. S. Muthu, and A. K.Sood, *Appl. Phys. Lett.*, **60**, 2116, (1992).

9 V. Vezin, P. Goudeau, A. Naudon, A. Halimaoui, and G. Bomchil, *Appl. Phys. Lett.*, **60**, 2625, (1992).

10. A. Bensaid, G. Patrat, M. Brunel, F. de Bergevin, and R. Herino, *Solid State Comm.*, **79**, 923, (1991).

11. Y. H. Xie, W. L. Wilson, F. M. Ross, J. A. Mucha, E. A. Fitzgerald, J. M. Macaulay, and T. D. Harris, *J. Appl. Phys.*, **71**, 2403, (1992).

12. Z. Sui, P. P. Leong, I. P. Herman, G. S. Higashi, and H. Temkin, *Appl. Phys. Lett.*, **60**, 2086, (1992).

13. J. C. Tsang, M. A. Tischler, and R. T. Collins, *Appl. Phys. Lett.*, **60**, 2279, (1992).

14. R. Tsu, H. Shen, and M. Dutta, *Appl. Phys. Lett.*, **60**, 112, (1992).

15. Y. Arita, *J. Crystal Growth*, **45**, 383, (1978).

16. Y. Arita and Y. Sunohara, *J. Electrochem. Soc.*, **124**, 285, (1977).

17. C. Pickering, M. I. J. Beale, D. J. Robbins, P. J. Pearson, and R. Greef, *J. Phys. C: Solid State Phys.*, **17**, 6535, (1984).

18. E. Chason, T. M. Mayer, D. McIlroy, and C. M. Matzke, *Nucl. Inst. Meth. Phys. Res.*, **B80/81**, 742, (1993).

19. E. Chason and D. T. Warwick, Mat. Res. Soc. Symp. Proc., vol. 208, 351, (1991).

20. M. J. Kelly, T. R. Guilinger, S. S. Tsao, W. B. Chambers, G. J. Fischer, and R. R. Sippio, IEEE SOS/SOI Technology Conference, Stateline, NV, Oct. 3-5, 1989.

21. T. R. Guilinger, M. J. Kelly, and J. O. Stevenson, Proceedings of the First International Symposium on Electrochemical Microfabrication, Ed. by M. Datta, K. Sheppard, and D. Snyder, The Electrochemical Society, vol. 92-3, 1992.

22. L. G. Parratt, *Phys. Rev.*, **95**, 359, (1954).

FIGURE CAPTIONS

Figure 1. X-ray reflectivity, R, normalized by Fresnel reflectivity, R_F, for the porous silicon sample anodized for 188 sec. Also shown is the non-linear least squares fit of the data using a single layer model.

Figure 2. Porous silicon thickness as a function of anodization time measured by X-ray reflectivity, XTEM, and gravimetry. Error bars on the X-ray reflectivity are 5% of the measured value. Error bars on the XTEM are estimated from maximum deviations of the measured thickness from the mean. Line for the X-ray reflectivity is linear least squares fit.

Figure 3. Cross-section TEM micrograph of the porous silicon sample anodized for 188 sec.

Figure 4. Roughness of the porous silicon/silicon interface and the porous silicon top surface as measured by X-ray reflectivity, XTEM, and atomic force microscopy (AFM). Lines are linear least squares fit.

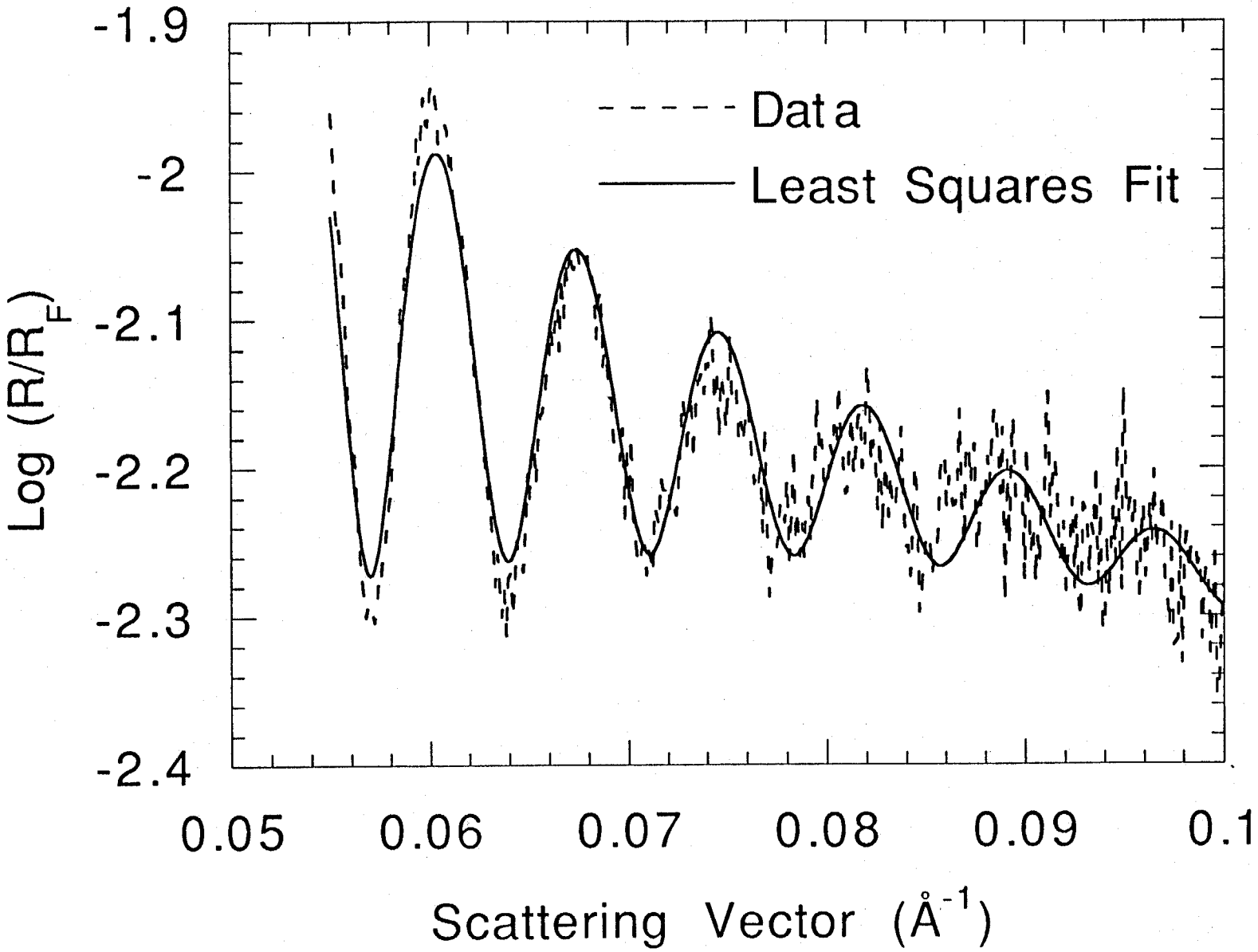
-1.9
-2
-2.1
-2.2
-2.3
-2.4
Log (R/R_F)
Data
Least Squares Fit
0.05
0.06
0.07
0.08
0.09
0.1
Scattering Vector (Å^-1)

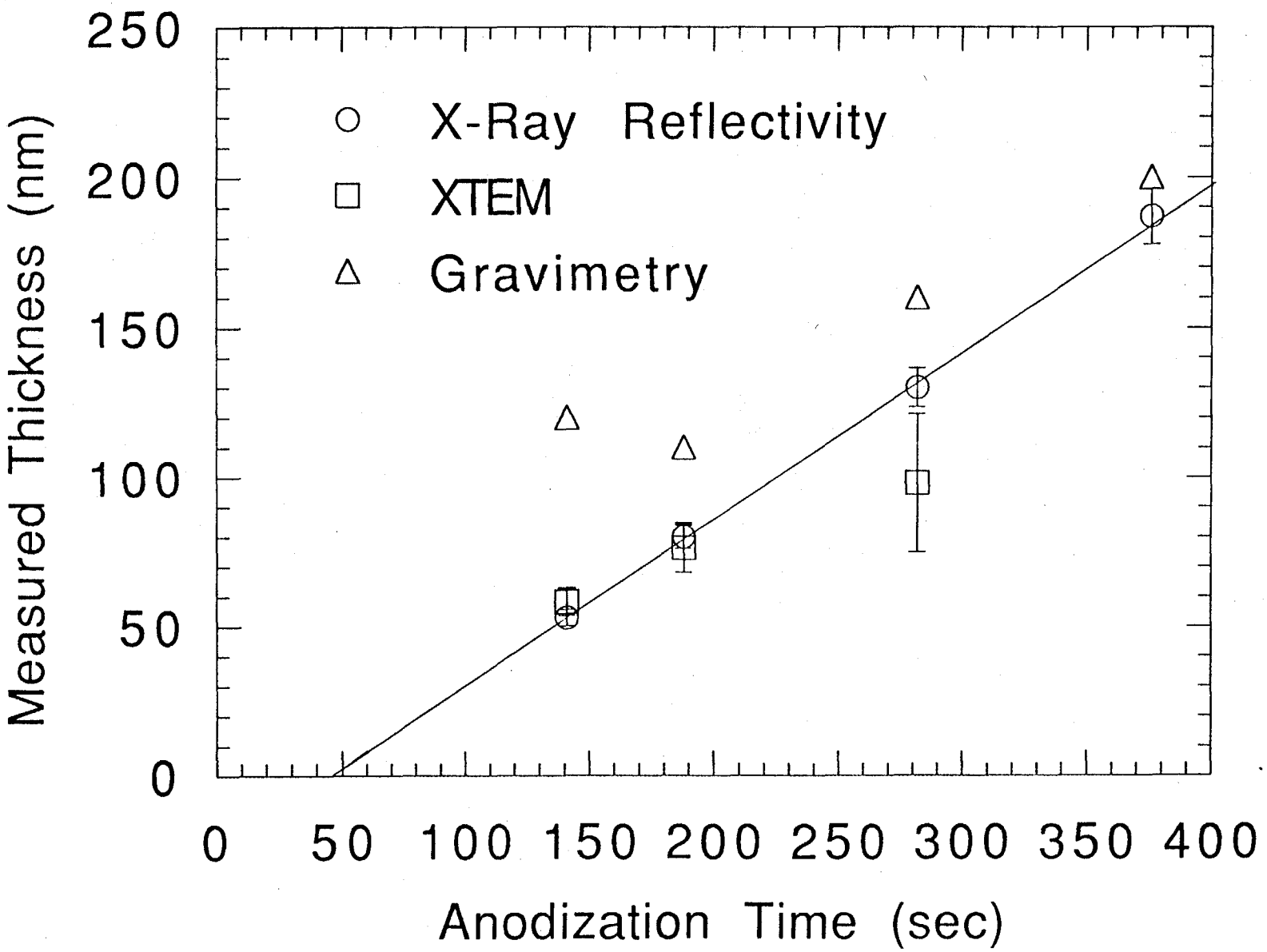
250
200
150
100
50
0
Measured Thickness (nm)
X-Ray Reflectivity
XTEM
Gravimetry
0
50
100
150
200
250
300
350
400
Anodization Time (sec)

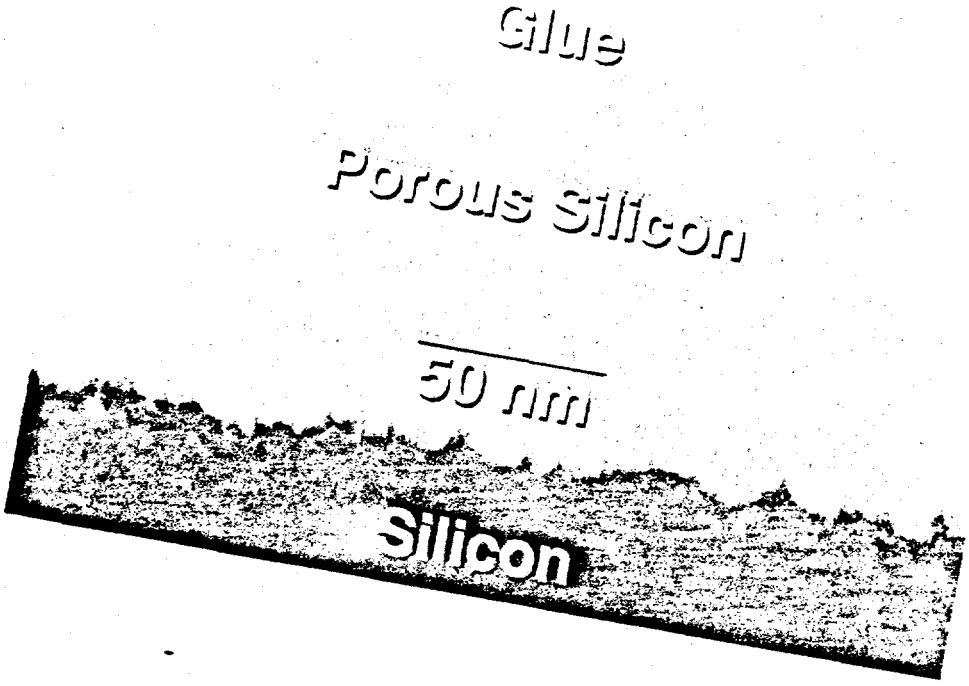
Glue
Porous Silicon
50 nm
Silicon

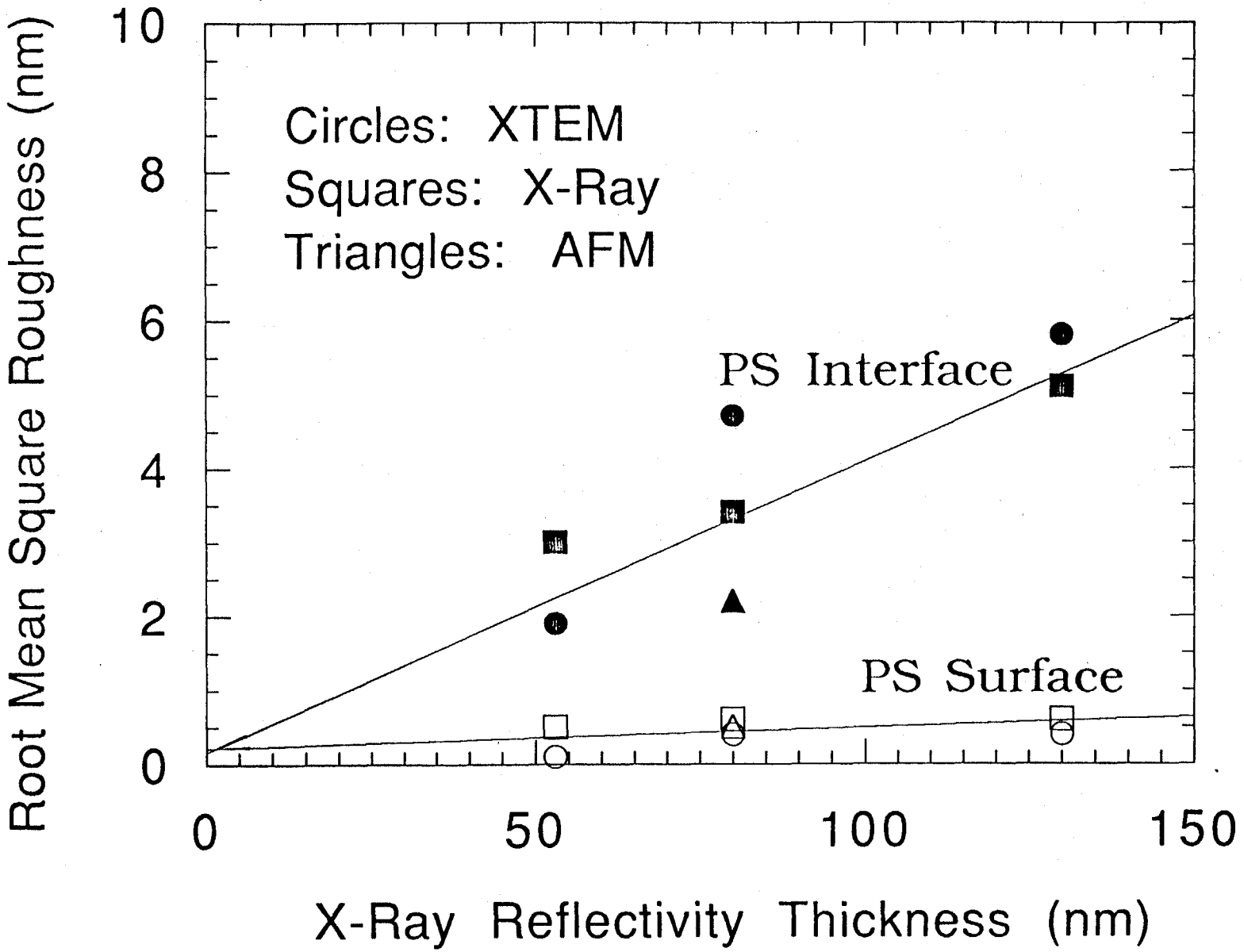
Root Mean Square Roughness (nm)
10
8
6
4
2
0
Circles: XTEM
Squares: X-Ray
Triangles: AFM
PS Interface
PS Surface
0
50
100
150
X-Ray Reflectivity Thickness (nm)

Appendix III. "Non-Destructive Characterization of Porous Silicon Using X-Ray Reflectivity"

NON-DESTRUCTIVE CHARACTERIZATION OF POROUS SILICON USING X-RAY REFLECTIVITY

E. CHASON, T.R. GUILINGER, M.J. KELLY, T.J. HEADLEY and A.J. HOWARD
Sandia National Laboratories, Albuquerque, NM 87185

ABSTRACT

Understanding the evolution of porous silicon (PS) layers at the early stages of growth is important for determining the mechanism of PS film growth and controlling the film properties. We have used X-ray reflectivity (XRR) to determine the evolution of layer thickness and interfacial roughness during the growth of thin PS layers (< 200 nm) prepared by electrochemical anodization. The porous layer grows at a constant rate for films as thin as 15 nm indicating a very short incubation period during which the surface may be electropolished before the PS structure begins to form. Interface roughness measurements indicate that the top surface of the film remains relatively smooth during growth while the roughness of the PS/silicon interface increases only slightly with film thickness. The XRR results are compared with results obtained from the same films by cross-sectional transmission electron microscopy (XTEM), atomic force microscopy (AFM) and gravimetry.

INTRODUCTION

Porous silicon (PS) films have properties that make them interesting for a variety of technological applications, e.g., as insulating layers in microelectronics [1] and for micromachining applications [2]. The discovery of visible photoluminescence by Canham [3] has generated further interest because of the possibility of creating light emitting devices in Si-based materials. Although there has been significant interest in utilizing PS, there is still not a complete understanding of the porous layer formation process or the resulting microstructure. Part of the reason for this is the difficulty of characterizing the porous structure accurately. Many of the available techniques are time-consuming and sample preparation can be difficult.

In this paper, we report on the use of X-ray reflectivity (XRR) to study the evolution of the PS film structure. XRR is a sensitive probe of thin film layer thickness and surface and interface roughness. The technique is non-destructive, requires minimal sample preparation and, because X-rays are highly penetrating, it is possible to study buried interfaces. We have concentrated primarily on the evolution of the PS film structure during the very early stages of film formation by measuring a series of samples prepared under identical condition for different anodization times. For comparison of the resolution of XRR with other techniques, some of the samples were also measured using gravimetry, XTEM and AFM.

The porous silicon (PS) was formed by electrochemical anodization of 0.5-1.0 Ω-cm, boron-doped, (100) p-Si in a dual tank electrochemical cell. Details of the design and testing of this cell are given elsewhere [4]. The PS samples were formed in 5 wt% HF at 0.58 mA/cm^2 for times ranging from 5 to 376 s. The total area of PS formed was 45.8 cm^2.

X-RAY REFLECTIVITY (XRR)

X-ray reflectivity is a technique for measuring the structure of thin films. A review of the technique may be found in ref. 5, so only a brief discussion is given here. The reflectivity is measured as a function of the scattering vector,

$$k = 4\pi/hc\ E \sin\theta \qquad (1)$$

where E is the energy of the X-ray and 2θ is the scattering angle. In contrast with X-ray diffraction, X-ray reflectivity is performed at small values of k where the reflectivity may be interpreted as arising from a continuous medium with an index of refraction, n, that depends on the electron density, ρ_{el} [6]. The index of refraction for X-rays in matter is less than 1 so that for sufficiently small incident angles total external reflection occurs.

Above the critical value for total external reflection (k_c), the reflectivity from an ideal interface is given by the Fresnel reflectivity ($R_F(k)$) with the asymptotic form $(k/k_c)^{-4}$. For an imperfect interface, the reflectivity is given approximately by [5]

$$R(k) = R_F(k)\,|\,F(d\rho_{el}/dz)|^2 \qquad (2)$$

where $F(d\rho_{el}/dz)$ is the Fourier transform of the electron density gradient in the direction normal to the surface of the film. The relationship between the film structure and eq. (2) is shown schematically in figure 1. The electron density in the direction normal to the film surface (fig. 1a) is constant where the film composition is uniform and changes at the interfaces between the substrate, the PS film and vacuum. The gradient of the electron density ($d\rho_{el}/dz$) has peaks at these interfaces as shown in fig. 1b. If the interface is smooth, then the peak in $d\rho_{el}/dz$ will be narrow, while if the interface is rough or diffuse, the peak will be broader. The roughness is generally taken to have a Debye-Waller form ($\exp(-k^2\sigma^2)$) where σ is the interface roughness. The normalized reflectivity from this structure (fig. 1c) is given by the Fourier transform of the density gradient. The oscillations shown in the reflectivity spectra come from interference between scattering from the surface and the buried interface, while the decay in the reflected intensity is determined by the roughness of the interfaces. The reflectivity spectra can therefore be analyzed to obtain the thickness, electron density and interface roughness of the individual layers.

The details of the experimental apparatus are discussed in ref. 7. In the energy dispersive technique used in this work, a broad range of X-ray energies impinge on the sample at a fixed angle and a solid-state Ge detector is used to simultaneously measure the reflectivity at each

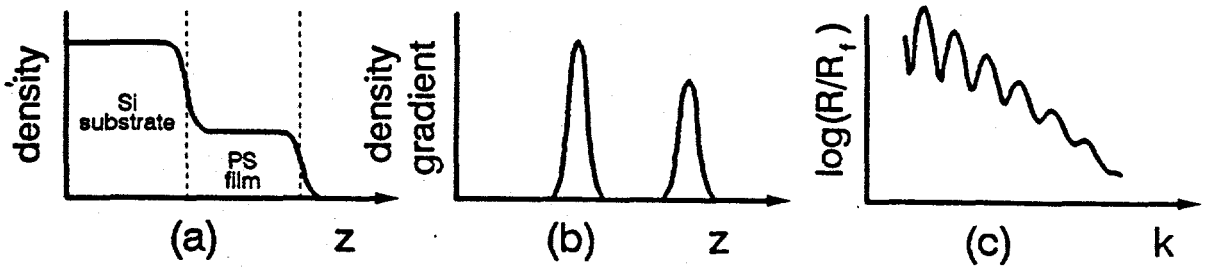

Figure 1. Schematic of relationship between a) electron density of thin film on substrate, b) electron density gradient normal to the surface and c) normalized X-ray reflectivity. z and k are in the direction normal to the surface of the film.

wavevector k. For the actual data analysis, an optical multilayer theory [8] that takes into account multiple scattering is used. Optimum values of parameters corresponding to porosity, PS layer thickness, surface roughness and buried interface roughness were obtained using a non-linear least-squares fitting routine. It is important to note that XRR only measures variations in the electron density normal to the film surface and does not probe the interface structure in the plane of the film. The total area of the sample illuminated by the X-ray beam is approximately 0.5 x 0.5 cm^2; the measured roughness corresponds to integrating over a region determined by the lateral coherence length of the X-rays which is on the order of 1 μm.

XRR spectra are shown in figure 2 from PS samples prepared for anodization periods of 5, 15, 30, 60 and 140 s as indicated in the figure. The increase in the frequency of the intensity oscillations with the anodization time corresponds to increasing layer thickness. The oscillations decay after only a few periods indicating substantial roughness at one or both of the interfaces. The solid lines represent the calculation of the reflectivity from the optical multilayer theory. For the sample that was processed for 5 s, the structure could be adequately described by a model that contained only a rough surface and no PS layer. For the other samples, a model structure containing a single PS layer on the Si substrate was used.

The dependence of the thickness of the PS layer on the anodization time is shown in figure 3. The error in the XRR determination of layer thickness is estimated to be ± 5%. The evolution of the roughness with anodization time is shown in figure 4a for the roughness from the surface and in figure 4b for the buried PS/substrate interface . The error on the surface roughness is estimated to be ± 0.2 nm while the error on the buried interface roughness is ± 0.5 nm. The solid lines in figures 3 and 4 are guides to the eye.

In the following section, we present a comparison between results obtained using XRR and other thin film analytical techniques. The implications of these results for understanding the growth process will be discussed in the final section.

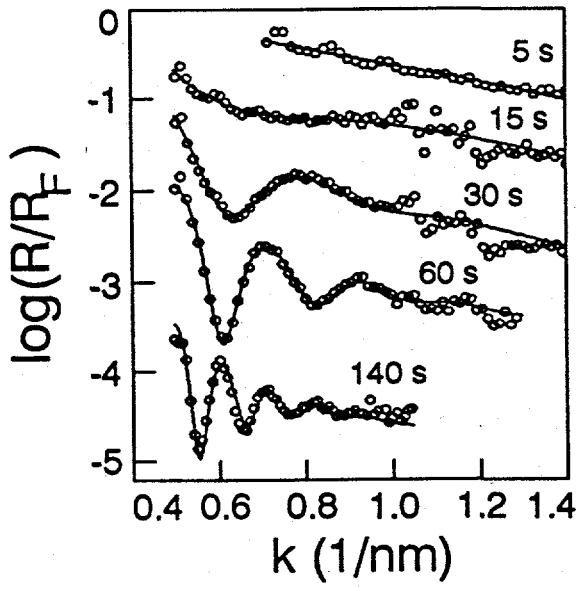

Figure 2. X-ray reflectivity spectra from PS films. Open circles are experimental data; solid lines are calculations from optical multilayer theory. Anodization times are indicated on the figure.

COMPARISON OF XRR AND OTHER EXPERIMENTAL TECHNIQUES

In order to compare the sensitivity of the XRR technique to other thin film analytical methods, a series of samples were prepared with different anodization times and analyzed using XRR, XTEM, AFM and gravimetry. An XTEM micrograph for a sample that was anodized for

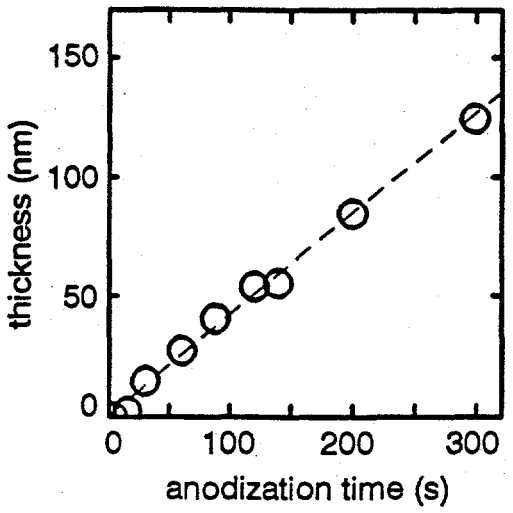

Figure 3. PS layer thickness vs. anodization time as determined by XRR.

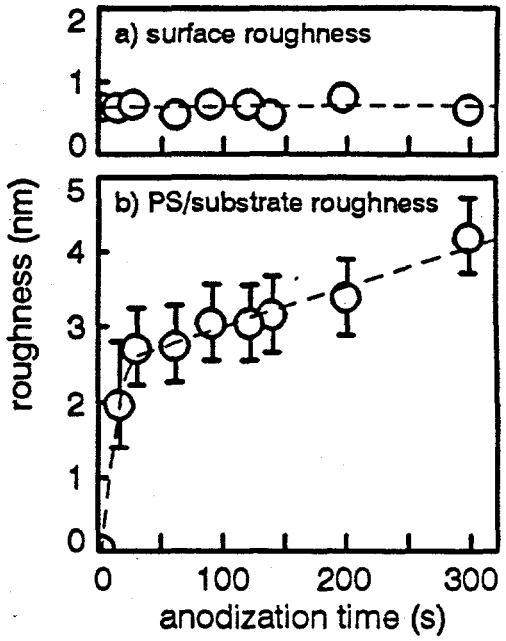

Figure 4. Development of a) surface roughness and b) PS/substrate interfacial roughness with anodization time as determined by XRR.

141 s is shown in figure 5. The micrograph was digitized and the average PS layer thickness and RMS roughness at the surface and buried interface was calculated. The lateral range covered by the micrograph was approximately 500 nm, which is comparable to the lateral coherence length of the XRR method. The micrograph indicates that the bottom interface is significantly rougher than the top surface. The image also shows no gross non-uniformities in the layer which is consistent with the good agreement of the XRR spectra with a single layer model.

Gravimetric measurements of layer thickness and porosity are obtained by measuring the change in the sample weight before and after PS layer formation and after stripping off the PS layer using NaOH. The porosity measurements (not shown) indicate that the porosity of the PS layer does not increase significantly with increasing layer thickness. The porosity of these films was on the order of 70 - 80%. The XRR results are consistent with the porosity of the films being independent of the layer thickness, but forcing the layer density to the value obtained from gravimetry produced significantly worse fits and suggests that the layer density may not be completely uniform with depth. AFM measurements of the surface roughness were obtained from analysis of several 1 μm x 1 μm regions per sample. The buried interface roughness was obtained by imaging the surface after stripping off the PS layer with 7M NaOH.

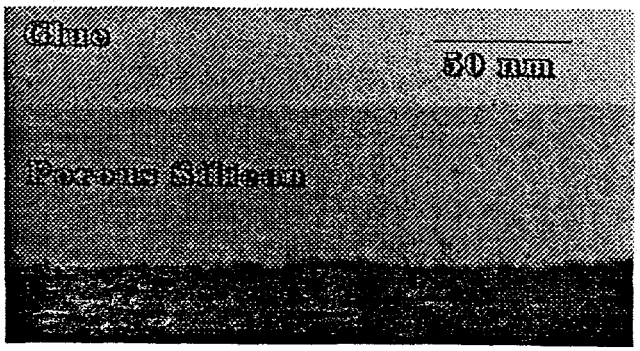

Figure 5. Cross-sectional TEM micrograph of PS film after 141 s anodization time.

The results for the layer thickness determination are shown in figure 6. The thicknesses calculated by gravimetry are consistently higher than for the XRR and XTEM. At small values of the layer thickness, the agreement of the gravimetry results becomes worse. For these very small layer thicknesses, the measurement is presumably dominated by the resolution of the weight change measurement. The agreement between the XRR and XTEM determinations of the sample thickness is very good. The main drawback to the XTEM analysis is the difficulty of preparing cross-sectional samples for analysis. Because XTEM samples a very small portion of the sample, local variations in the thickness can have a significant effect on the errors associated with the measurement.

A comparison of the measured surface and interface roughness is shown in figure 7 for the surface (figure 7a) and the PS/substrate interface (figure 7b). All of the techniques indicate that the bottom interface is significantly rougher than the surface and are in approximate agreement on the magnitude of the interfacial (2 - 5 nm) and surface (0.5 nm) roughness. Although XTEM suggests a stronger dependence of the bottom surface roughness on anodization time than the XRR, the small area of the sample used for XTEM measurements makes it difficult to determine what error should be associated with this number. The AFM value of the bottom surface roughness also may be supressed due to smoothing of the interface during the PS removal with NaOH.

EVOLUTION OF THIN FILM STRUCTURE

The results of the XRR measurement of PS layer thickness (figure 3) indicate that the layer formation rate is linear with time even for very thin layers. Significant deviation from linearity occurs only for the results obtained at the shortest anodization times: 5 s, where no PS layer is observed, and 15 s where the measured thickness falls below the linear value extrapolated from the longer times. These results suggest that the growth is linear except when the layer thickness is comparable to the roughness of the bottom interface.

The evolution of the surface roughness with anodization time (figure 4) indicates that once the initial pore formation is completed, the top surface does not continue to etch significantly.

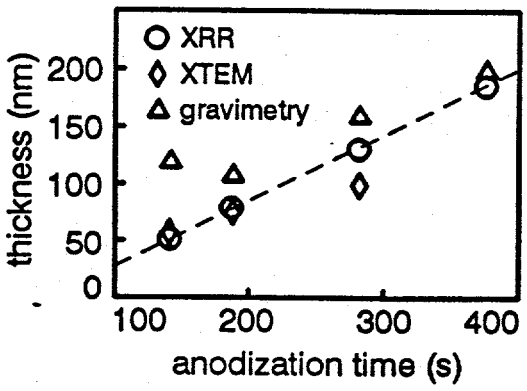

Figure 6. Comparison of PS film thickness determined by XRR, XTEM and gravimetry.

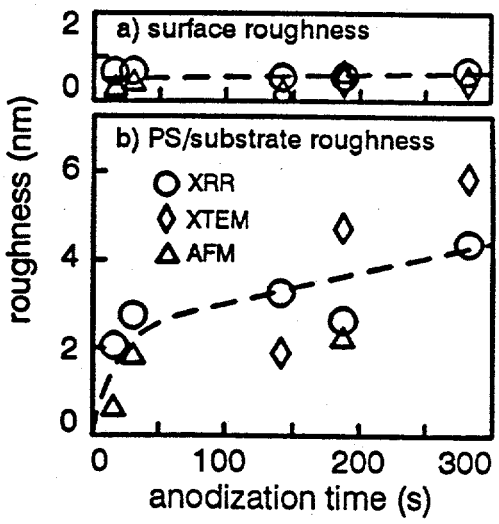

Figure 7. Comparison of a) surface roughness and b) PS/substrate interfacial roughness determined by XRR, XTEM and AFM.

The surface reaches a roughness of between 0.5 - 0.7 nm after only 5 s, and this roughness does not increase over the measured range. This result is consistent with the gravimetric result that indicates that the porosity does not change after the initial porous layer is formed. If the porosity were changing significantly, it would most likely lead to an increase in the surface roughness as well. Etching of the Si by HF does not appear to contribute to a significant increase in the surface roughness. At an estimated etch rate of 0.0005 nm/s [9], only 0.15 nm of Si is removed after the maximum etch time of 300 s which is significantly less than the surface roughness of 0.6 nm.

The fact that the roughness of the buried interface does not increase significantly suggests that the PS forming reaction is self-limiting, i.e., that the pores interact to keep the growth front at the same level. This is consistent with previous work performed on the effect of PS formation on initially rough substrates in which it was found that the porous layer formation resulted in a buried interface that was smoother than the intial surface roughness [10].

These results are consistent with a model that suggests that for very early times, the porous layer starts to form by initially roughening the top surface. This porous layer is formed very shortly after the etching process begins since we do not observe a long incubation period of electropolishing before the PS layer formation begins. The Si appears to be significantly etched only in the vicinity of the pore tips since the top surface does not continue to roughen after the PS layer is formed. The active region of pore formation has a width of approximately 3 nm which it maintains as it continues to burrow into the Si substrate. Since these results are taken from the very early stages of layer formation, it is difficult to compare with the predictions of proposed models of PS formation that deal primarily with the later stages of growth [11].

In conclusion, we have used X-ray reflectivity to study the evolution of PS layer thickness, surface roughness and PS/substrate interface roughness. The results obtained with XRR are in good agreement with results obtained by gravimetry, XTEM and AFM. The growth kinetics indicate that the rate of PS formation is remarkably linear beyond the point where the layer thickness is comparable to the steady-state roughness of the PS/substrate interface. The surface and buried interface roughness remain constant during the PS layer growth with the buried interface rougher than the surface by a factor of 5. This work was performed at Sandia National Laboratories supported by the U. S. Department of Energy under contract DE-ACO4-94AL85000.

REFERENCES

1. S.S. Tsao, IEEE Circuits Devices **CD-3**, 3 (1987).
2. P. Steiner, A. Richter and W. Lang, J. Micromech. Microeng. **3**, 32 (1993).
3. L.T. Canham, Appl. Phys. Lett. **57**, 1046 (1990).
4. T.R. Guilinger, M.J. Kelly and J.O. Stevenson, *Proc. of the First Int'l. Symposium on Electrochemical Microfabrication*, edited by M. Datta, K. Sheppard and D. Snyder, The Electrochemical Society, vol. 92-3, 1992.
5. J. Als-Nielsen in *Structure and Dynamics of Surfaces*, edited by W. Schommers and P. von Blanckenhagen (Springer, Berlin, 1986), Chap. 5, p. 181.
6. J.H. Underwood and T.W. Barbee, Appl. Opt. **20**, 3027 (1981).
7. E. Chason, T.M. Mayer, A. Payne and D.T. Wu, Appl. Phys. Lett. **60**, 2353 (1992).; E. Chason and D.T. Warwick, Mat. Res. Symp. Proc. Vol **208**, 351 (1991).
8. L.G. Parratt, Phys. Rev. **95**, 359 (1954).
9. S.M. Hu and D.R. Kerr, J. Electrochem. Soc. **114**, 414 (1967).
10. T.R. Guilinger and M.J. Kelly, unpublished result.
11. R.L. Smith and S.D. Collins, J. Appl. Phys. **71**, R1 (1992).

Appendix IV. "Reciprocal Space Analysis of the Microstructure of Luminescent and Non-Luminescent Porous Silicon Films"

RECIPROCAL SPACE ANALYSIS OF THE MICROSTRUCTURE OF LUMINESCENT AND NONLUMINESCENT POROUS SILICON FILMS

S.R. LEE, J.C. BARBOUR, J.W. MEDERNACH, J.O. STEVENSON AND J.S. CUSTER
Sandia National Laboratories, Albuquerque, NM 87185

ABSTRACT

The microstructure of anodically prepared porous silicon films was determined using a novel x-ray diffraction technique. This technique uses double-crystal diffractometry combined with position-sensitive x-ray detection to efficiently and quantitatively image the reciprocal space structure of crystalline materials. Reciprocal space analysis of newly prepared, as well as aged, p^- porous silicon films showed that these films exhibit a very broad range of crystallinity. This material appears to range in structure from a strained, single-crystal, sponge-like material exhibiting long-range coherency to isolated, dilated nanocrystals embedded in an amorphous matrix. Reciprocal space analysis of n^+ and p^+ porous silicon showed these materials are strained single-crystals with a spatially-correlated array of vertical pores. The vertical pores in these crystals may be surrounded by nanoporous or nanocrystalline domains as small as a few nm in size which produce diffuse diffraction indicating their presence. The photoluminescence of these films was examined using 488 nm Ar laser excitation in order to search for possible correlations between photoluminescent intensity and crystalline microstructure.

INTRODUCTION

The goals of this study were two-fold. The first was to assess the ability of a relatively new technique for reciprocal space analysis, based on position-sensitive x-ray detection, to yield new insights into the crystalline microstructure of various types of porous silicon. In order to do this, reciprocal space analysis was used to survey the microstructure of both newly prepared and aged porous silicon films anodized under a variety of conditions. Perhaps not surprisingly -- given the wide range of conclusions reached in transmission electron microscopy (TEM), transmission electron diffraction and x-ray diffraction studies that are already published -- the porous silicon studied here was found to exhibit a wide range of crystallinity and a diverse microstructure. Using reciprocal space analysis, we found that we could observe and quantify the following microstructural phenomena: nanocrystal and nanovoid size and shape, nanocrystal orientation, lattice dilation in films containing isolated nanocrystals, lattice strain distributions in films which remain single crystalline, and mean pore spacing in single-crystalline samples containing vertical pore arrays. Results for three prototypical porous silicon structures are presented in detail below in order to demonstrate the unique capabilities offered by reciprocal space analysis.

Quantitative determinations of the size, shape and volume-fraction of nanocrystalline domains that exist in various forms of porous silicon are of particular interest because of their relevance to quantum confinement as a mechanism for photoluminescence (PL) in porous silicon. Our second goal was to attempt to test the quantum confinement hypothesis by looking for the presence or absence of a quantitative correlation between relative PL efficiency and relative nanocrystal density. Thus, following structural characterization by reciprocal space analysis, photoluminescence measurements were made on all samples. While our comparisons of photoluminescence and microstructural results are not yet on a fully quantitative footing, an initial discussion of photoluminescence and microstructural results is presented.

EXPERIMENTAL

(100)-oriented, 625 μm-thick Si wafers that were doped n^+, p^+ or p^- were anodized at constant current. The electrochemical cell was a bowl-type arrangement with a Au-plated metal platen contacting the Si backside to form an anode at the bottom of the cell. A Pt mesh was suspended above the Si as the cathode. A schematic of the cell appears in reference [1]. The samples for which we present detailed reciprocal space analysis results were anodized in (1:1) HF:ethanol. Additional specific details for the anodization of each sample are presented below.

Reciprocal space analysis of the porous Si was carried out using an apparatus that consists of a standard, double-crystal, x-ray diffractometer which has been modified by the addition of a position-sensitive x-ray detector (PSD) [2-4]. The PSD simultaneously measures the total scattering angle of diffracted x-rays emerging from the sample over a wide range of 2θ angles. This highly parallel analysis of the scattering angle allows one to map reciprocal space more than 100 times faster than can be done using a traditional, serially-scanned, triple-axis diffractometer. The tradeoff is a substantial decrease in resolution relative to that of a triple-axis system [4]. Reciprocal space maps were produced by measuring the diffracted x-ray intensity as a function of the rocking angle of the sample, ω, and the scattering angle, 2θ. Intensity as a function of angle, I(ω,2θ), was then mapped into an intensity function in reciprocal space, I(K[00l],K[hh0]), using a coordinate transformation derived from an Ewald sphere construction [3].

The photoluminescent signal was excited by 488 nm wavelength light from a multi-mode Ar laser. The excitation light was incident at 45° from the sample normal, and the PL light was collected at an angle of 10° from the sample normal in an optical fiber. The illumination spot-size was ≈ 1 mm in diameter, and the power density was ≈ 1.5 W/cm^2. The emitted PL light was analyzed using a monochromator with a 150 groove/mm grating and detected with a thermoelectrically-cooled CCD photodetector. The resolution of this system was measured to be 2.3 nm over the range of wavelengths for the porous silicon light emission. Illumination times varied from 1-100 seconds depending on luminescent intensity.

RECIPROCAL SPACE ANALYSIS RESULTS

Figure 1 shows reciprocal space maps for (004) and (224) diffraction from a 0.78 Ω-cm, p-type sample, produced by anodization at 80 ma/cm^2 for 5 minutes. The sample is 20 μm thick and has a porosity of 69%. For this sample, diffraction and PL results were collected after the sample was stored in air for more than one year. The diffraction patterns of Figure 1 are consistent with a microstructure made of isolated nanocrystals dispersed in an amorphous matrix.

The intense center spot in Figures 1(a) & 1(b) is due to substrate diffraction. The extended diagonal streak in each figure is an artifact produced by reducing the diffractometer power as the scan rocks through the intense substrate peak. This is required in order to avoid damage to the PSD. This streak fortuitously marks the orientation of the Ewald sphere in each scan.

The important feature in Figure 1 is the diffuse pattern surrounding the substrate peak. This intensity consists of two components: thermal diffuse and background scattering from the substrate, and nanocrystal diffraction in the porous layer. The broadening of the diffuse intensity along K[hh0] in Figure 1(a), and its rotation between (004) and (224) so that it remains normal to an axis passing through the origin of reciprocal space, is consistent with the presence of nanocrystals that are slightly misoriented with respect to the substrate. The width along K[hh0] in Figure 1(a) indicates that the nanocrystals are tilted away from the substrate [001] axis by < 1.6°.

Figure 2 shows the same data as in Figure 1(a) minus the large background due to substrate scattering. This residual intensity is due only to nanocrystalline scattering in the porous layer.

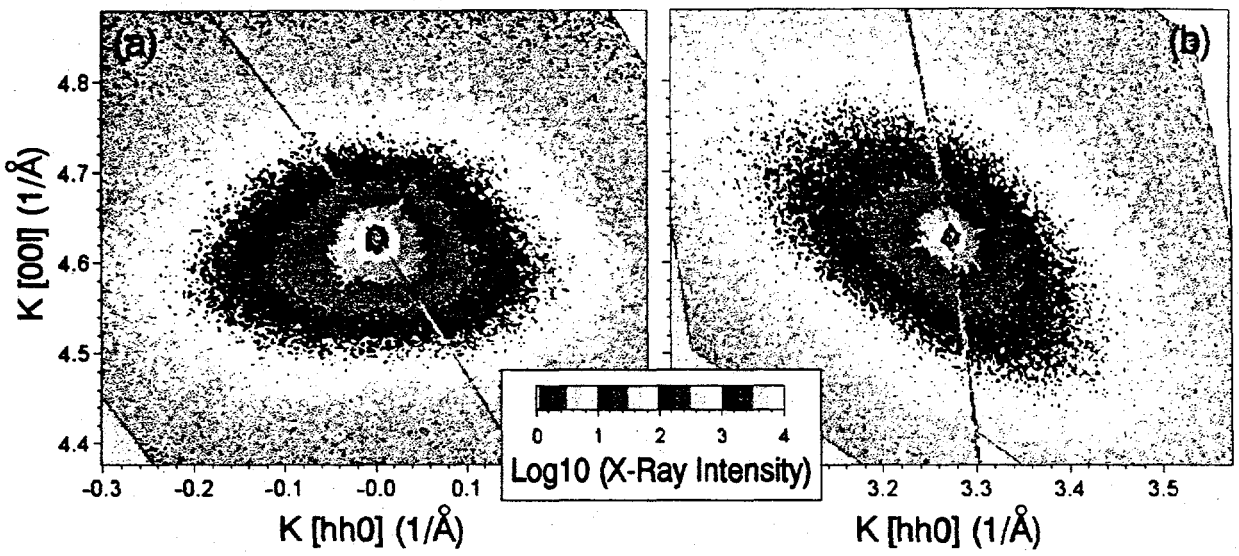

Figure 1. (a) the (004) diffraction pattern, and (b) the (224) diffraction pattern produced by p⁻ porous Si composed of isolated nanocrystals embedded in an amorphous matrix.

Using the width of this intensity peak along the K[00l] direction and the Scherrer particle size formula, or by direct comparison with reciprocal space simulations based on the kinematic theory of diffraction by small crystals [5], these nanocrystals are found to be 3-5 nm in diameter. Taking into account the broadening of the intensity distribution along K[hh0] due to misorientation effects, the reciprocal space intensity is approximately spherical. This indicates that on average these nanocrystals are spherical in shape. Finally, the vertical shift in the centroid of the peak to a K[00l] coordinate smaller than that of the substrate indicates that the nanocrystal lattice has dilated. The average nanocrystal perpendicular lattice constant is found to be 5.470 Å. Assuming a cubic dilation, based on similar asymmetries in the (004) and (224) diffuse scattering shown in Figure 1, a dilation of 0.72% is obtained. This agrees quite well with previous measurements where dilations of 0.65% [6] and 0.95% [7] were found for Si nanocrystals 4 nm in diameter.

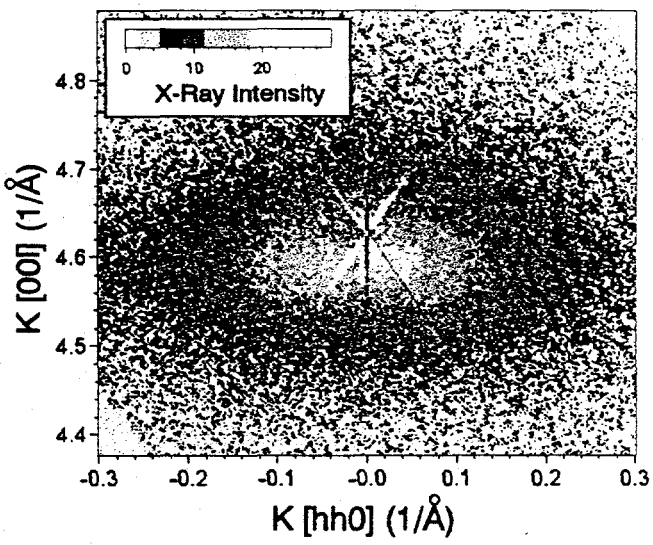

Figure 2. The (004) diffraction pattern produced by p⁻ porous Si, after subtraction of substrate background scattering, showing dilation of the nanocrystal lattice.

As a second example of reciprocal space analysis of porous silicon, figure 3 shows reciprocal space maps for (004) and (224) diffraction from a 0.86 Ω-cm, p-type sample, produced by anodization at 80 ma/cm^2 for 30 minutes. This sample is 120 μm thick and has a porosity greater than 69%. In this case, diffraction and PL results were collected after the sample was stored in air for about four days. At first glance, the intense diffuse scattering, the large width of the diffuse intensity along K[00l], and the rotation of the diffuse intensity on going from (004) to (224) again suggests nanocrystals that are a few nm in diameter. However, in

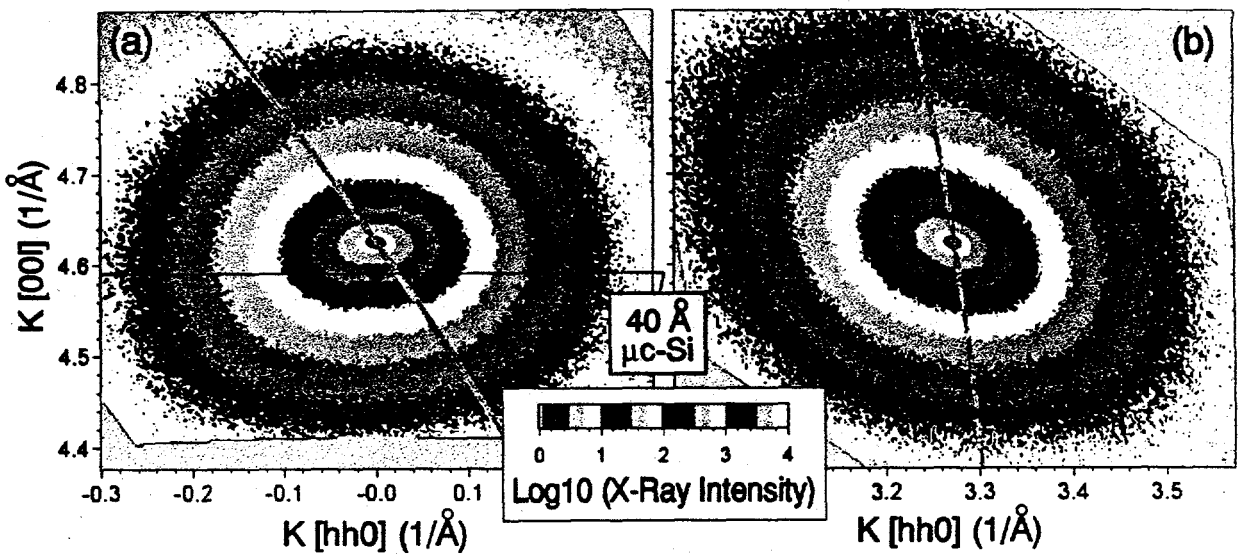

Figure 3. (a) the (004) diffraction pattern, and (b) the (224) diffraction pattern produced p^- porous Si composed of a single-crystal sponge and misoriented, sponge-like domains a few tens of nm in size.

Figure 3(a) we have marked the expected centroid position due to diffraction by dilated, 4-nm-diameter nanocrystals. The observed diffraction pattern is symmetrically centered about the Si substrate peak, and there is no distortion of the pattern in the direction of the expected dilation. This is inconsistent with a dilated, few-nm-diameter, nanocrystalline picture of microstructure.

In contrast to the aged p^- sample discussed above, combined (004) and (224) rocking curve results (not shown) reveal that a coherently strained, crystalline sponge comprises at least a portion of this anodized layer. The intensity of the layer's strain peak was weak (30x smaller than the substrate peak) despite the large thickness of the anodized layer. This may be because this coherently diffracting domain is a thin portion of the entire layer, or it may result from a thicker, but highly disordered layer that retains only partial coherency. This layer has a parallel lattice constant equal to that of bulk silicon and is tetragonally distorted in the surface normal direction by 0.06%. The lattice is slightly dilated in agreement with previous studies [8,9].

Returning now to the diffuse scattering patterns of Figure 3, the following microstructural picture is offered as a possible explanation. Domains of the crystalline sponge a few tens of nm in size are misoriented with respect to the main structure. As before, the fact that the diffraction pattern remains normal to an axis going through the origin of reciprocal space for both (004) and (224) diffraction is consistent with rigid rotation of the domains away from their original orientation. The width of the intensity distribution in Figure 3(a) along K[hh0] suggests misorientations up to 0.7°. Since these domains are ≈ 10 nm in size or larger, a large lattice dilation is not expected, and the intensity remains centered about the substrate peak. Because the domains are rather large, this only explains the diffuse scattering for ΔK values within about 0.06 $Å^{-1}$ of the substrate peak (ΔK is distance in reciprocal space relative to the substrate reciprocal lattice point). Intensity at larger ΔK arises due to scattering from the randomly positioned, 2-5 nm diameter *voids* which permeate both the coherent, and the misoriented, sponge-like domains.

As a final example of reciprocal space analysis, Figure 4 shows results for (004) and (224) diffraction from a 0.013 Ω-cm, n-type sample, produced by anodization at 60 ma/cm^2 for 30 minutes. The sample is 95 μm thick and has a porosity of 48%. Here, diffraction and PL results were collected after the sample was stored in air for three days. For both the n^+ and p^+ material we examined, there was always an intense coherent diffraction peak located near the substrate

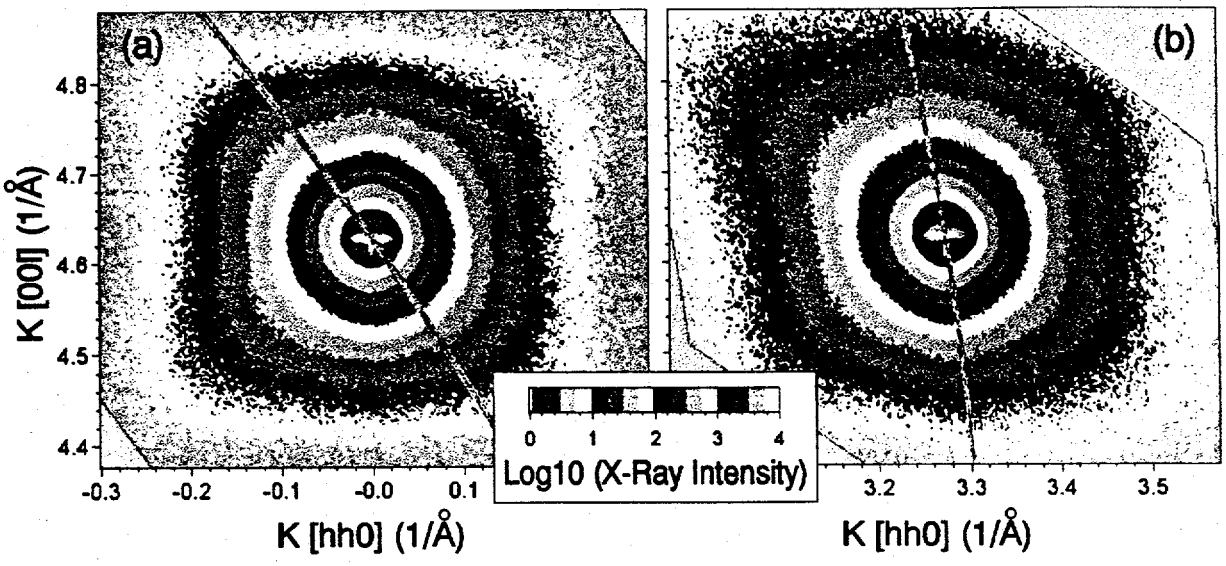

Figure 4. (a) the (004) diffraction pattern, and (b) the (224) diffraction pattern produced by n^+ porous Si composed of a single crystal layer penetrated by an vertical array of pores. Diffraction from nanovoids adjacent to the main pores appear to explain these patterns.

diffraction peak, indicating that these materials are primarily slightly strained single-crystals. The dense array of vertical pores in these samples produces a crossbar of intensity centered on the strain peak. This crossbar is barely seen near the center of Figures 4(a) and (b). Bensaid et al. [10] provide both an explanation for the crossbar intensity based on correlated spacing of the pores and a brief discussion of diffraction by randomly positioned voids.

In Figure 4, diffraction from nm-sized domains is again observed. In contrast to the above p^- results, the diffraction pattern does not change its basic orientation when going from (004) to (224) diffraction. This indicates that misoriented domains are not the main source of diffracted intensity for this sample. Here, the shape of the intensity distribution along K[00l], and the symmetry of the diffraction pattern, suggests scattering from approximately spherical domains 2-20 nm in size. However, since embedded nano*crystals* are expected to exhibit both appreciable misorientations and dilations that are not seen in Figure 4, it is believed that this diffraction pattern may again result from diffraction by nano*voids*. TEM of similar n^+ samples shows a graded structure with pores in the upper region being surrounded by nm-sized domains [11].

PHOTOLUMINESCENCE RESULTS

Photoluminescence spectra for the above samples appear in Figure 5 as curves (a), (b) and (e) along with spectra for two other samples we are studying. The same collection efficiency and pump power was used for each sample so that the spectral intensities could be compared.

First we consider p^- samples which contained dilated nanocrystals. The most intense PL signal (curve (a)) came from the aged p^- sample anodized at 80 ma/cm^2 (presented first above). This spectrum also exhibits strong intensity oscillations not seen in the other samples. These oscillations could be eliminated by tilting the sample to an 85° incident beam angle, or by using the 514 nm Ar line for excitation. Curves (c) and (d) in Figure 5 are for p^- samples anodized under much different conditions, but which also PL near 690 nm. Sample (c) produces a very weak, almost undetectable, nanocrystal diffraction pattern while sample (d) has a clear, but weak, nanocrystal diffraction pattern. Yet, these samples have PL integrated intensities that are 37% and 17%, respectively, of the intensity of curve (a). Superficially, there appears to be a lack of correlation between relative nanocrystal density and PL intensity that does not support

the quantum confinement mechanism for PL emission. However, these three samples have substantial differences in thickness, porosity, and perhaps nanocrystal size, that have not yet been fully determined. An ongoing part of the present work is to take these factors into account in order to more carefully extract relative nanocrystal densities from the reciprocal space maps. Ultimately, a quantitative comparison of nanocrystal density and PL intensity will be made.

Next, the 4-day-old, p^- sample which was structurally analyzed second above, and which is believed to be a crystalline sponge with misoriented domains a few tens of nm in size, luminesced strongly, but was red-shifted to 760 nm (Figure 5(b)). This PL result does not appear to be explained by a quantum confinement mechanism *unless* quantum confinement effects can occur in an extended, sponge-like, single-crystal structure ten or more nm on a side that is made up of smaller nm-sized interconnects. A possible complicating factor here is that the diffraction pattern produced by nanovoids in the sponge-like domains could be masking weaker diffraction by nanocrystals, which may be present at a lower number density. Again a more quantitative approach appears needed.

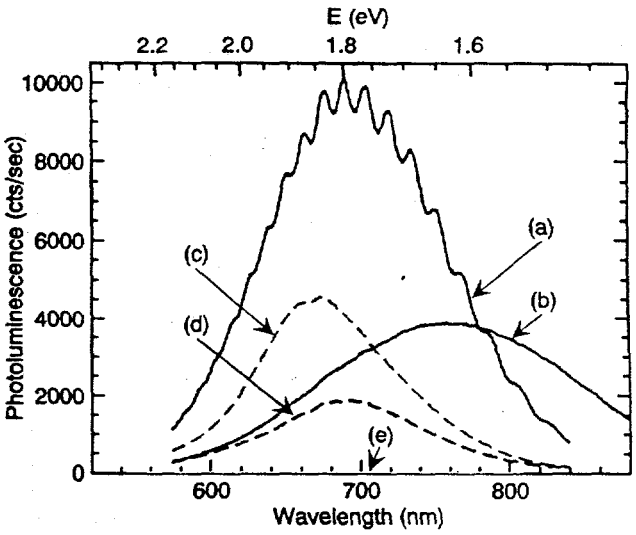

Figure 5. Photoluminescence spectra: (a) > 1-yr-old p^-, 80 ma/cm^2 in (1:1) HF:ethanol, (b) new p^-, 80 ma/cm^2 in (1:1) HF:ethanol, (c) > 1-yr-old p^-, 20 ma/cm^2 in (1:10) HF:H_2O, (d) new p^-, 10 ma/cm^2 in (1:10) HF:H_2O, (e) n^+ and p^+

Finally, none of the n^+ or p^+ samples that were examined luminesced above background. Moreover, these samples did not appear to contain dilated nanocrystals in the few-nm-size range.

REFERENCES and ACKNOWLEDGMENTS

This work was supported by the U.S. Department of Energy under contract DE-AC04-94AL85000 and was partially funded by the Sandia National Laboratories LDRD program.

[1] T.R. Guilinger, M.J. Kelly, J.O. Stevenson, A.J. Howard, J.E. Houston and S.S. Tsao, in Proceedings of the Electrochemical Microfabrication Symposium, The Electrochemical Society, Phoenix, AZ, Oct. 13-18, 1991.

[2] L.R. Thompson, G.J. Collins, B.L. Doyle and J.A. Knapp, J. Appl. Phys. **70**, 4760 (1991).

[3] S.T. Picraux, B.L. Doyle and J.Y. Tsao, in Semiconductors and Semimetals **33**, edited by T.P. Pearsall (Academic Press, Boston, 1991), pp. 139-220.

[4] S.R. Lee, B.L. Doyle, T.J. Drummond, J.W. Medernach and R.P. Schneider, Jr., to be published in Advances in X-Ray Analysis **38**, Proceedings of the 43rd Annual Conference on Applications of X-Ray Analysis, Steamboat Springs, CO, August 1-5, 1994.

[5] B. E. Warren, X-Ray Diffraction, (Addison-Wesley, Reading, MA, 1969) , pp. 27-30.

[6] M. Hamasaki, T. Adachi, S. Wakayama and M. Kikuchi, J. Appl. Phys. **49**, 3987 (1978).

[7] S. Veprek, Z. Iqbal, H.R. Oswald, F.-A. Sarott, J.J. Wagner and A.P. Webb, Solid State Commun. **39**, 509 (1981).

[8] K. Barla, R. Hérino, G. Bomchil and J.C. Pfister, J. Cryst. Growth **68**, 727 (1984).

[9] I.M. Young, M.I.J. Beale and J.D. Benjamin, Appl. Phys. Lett. **46**, 1133 (1985).

[10] A. Bensaid, G. Patrat, M. Brunel, F. de Bergevin and R. Hérino, Solid State Commun. 79, 923 (1991).

[11] J.W. Medernach and T.J. Headley (private communication).

Appendix V. "Visible Light Emission from Porous Silicon Examined by Photoluminescence and Raman Spectroscopy"

VISIBLE LIGHT EMISSION FROM POROUS SILICON EXAMINED BY PHOTOLUMINESCENCE AND RAMAN SPECTROSCOPY

TERRY R. GUILINGER, MICHAEL J. KELLY, DAVID R. TALLANT, DAVID A. REDMAN, AND DAVID M. FOLLSTAEDT
Sandia National Laboratories, Albuquerque, New Mexico 87185

ABSTRACT

We describe the acquisition of Raman and photoluminescence (PL) spectra on porous silicon (PS) samples that emit visible light. Spectra were acquired in both *ex situ* experiments (after exposure to air) and *in situ* experiments (with the PS covered either with the hydrofluoric acid electrolyte used in the formation process or water). Our results generally show a correlation of blue-shifted PL with increased oxidation. In one set of *ex situ* experiments, however, we observed an inconsistency in the shift of the wavelength of maximum luminescence intensity for PS samples that exhibit oxygenated character in the Raman spectra. A higher anodization current density produced a red shift in the PL spectra in one experiment, while chemical dissolution of the PS by hydrofluoric acid produced the well-known blue shift in the other case. In two *in situ* experiments, we observed very weak and red-shifted PL for a PS sample immersed in HF (compared to the same sample measured later in air) while in another we immersed air-exposed PS in water and observed a 15-fold increase in PL intensity along with a blue shift in the luminescence maximum.

INTRODUCTION

Although the property of visible luminescence from porous silicon (PS) was discovered more than 30 years ago [1], a renewed interest due to the work of Canham [2] has resulted in numerous publications examining the composition and morphology of PS and their relation to the mechanism of PS photoluminescence (PL). As yet, no clear model for PS photoluminescence has been accepted. Proposed mechanisms include: (1) quantum size effects in the PS nanostructures affecting the electronic band structure of silicon [2,3]; (2) luminescence from Si-O-H polymeric compounds such as siloxene, [4]; (3) PL due to the presence of SiH_x species, particularly SiH_2 [5]; and (4) light emission from hydrogen-terminated amorphous silicon structures [6].

Techniques such as Raman and Fourier-transform infrared (FTIR) spectroscopies have been used to examine the chemical species present in PS and associate these chemical species with PS photoluminescence. FTIR measurements of air-exposed PS films indicate that H-bonding to the Si yields SiH_x surface species that may be important in PS photoluminescence since the peak PL intensity increases with increasing SiH_x concentration [5]. Conversely, another FTIR study reports that the growth of a native oxide, and subsequent consumption of the SiH_x from the PS, alters only slightly the PL, thus precluding SiH_x as the species responsible for visible PL [7]. Another FTIR study demonstrated that the disappearance of the PL with annealing temperature did not scale directly with H_2 desorption and concluded that PL from PS is not directly related to the presence of SiH_x species on the PS surface [8].

Raman spectroscopy has been used to support the siloxene model of PS photoluminescence owing to the similarities between PS and siloxene spectra [4]. Other Raman measurements of PS samples exposed to air show a shift and broadening of the crystalline Si (c-Si) peak consistent with silicon nanocrystallites in the 2-6 nm range, and the absence of an amorphous silicon peak [9-11]. Shifting and broadening of the c-Si peak at 521 cm^{-1} has been correlated with Si nanocrystallite size thus affording a means for measuring the dimensions of Si nanostructures in PS [9,12].

It is our intent in this paper to show that we can utilize Raman and PL spectroscopy both *in situ* and *ex situ* to probe PS samples for evidence of SiH_x species, O-Si-H_x species, amorphous Si, and the shift in the crystalline silicon Raman peak associated with decreasing Si crystallite size in the 2-10 nm range. Because of the importance of the environment in determining the species on the chemically reactive PS

surface, the ability to record Raman and PL spectra in the presence of air (*ex situ* measurement) as well as in the anodization cell containing the hydrofluoric acid electrolyte or some other liquid without exposure to air (*in situ* measurement) is crucial to obtaining reliable correlations between the presence of chemical species in the PS and the energy and intensity of the photoluminescence.

EXPERIMENTAL

Porous silicon was formed by anodization of 4-inch diameter, 0.8-1.2 Ω-cm, boron-doped, (100) silicon in a spectroelectrochemical cell containing hydrofluoric acid (HF) electrolyte. The cell, fabricated from high-density polyethylene (HDPE), confines electrolyte to the front side of the wafer using 2 Viton o-rings. Electrical contact was made to the back side of the wafer using a platinum disk. A sapphire window was sealed against a Viton o-ring on the front of the cell body using a HDPE window cap bolted to the cell body. The distance between the silicon wafer and the inside surface of the sapphire window was 0.8 cm, and the area of the wafer exposed to the electrolyte was 38 cm^2. Electrolyte was introduced to the volume between the wafer and window using a syringe and 1/16 " teflon tubing connected to the cell body with teflon fittings. A platinum mesh next to the window served as the counter electrode. A 6 mm high opening was cut into the center of the mesh to allow access of the laser beam to the wafer surface. The generation of hydrogen bubbles at the silicon wafer and the platinum mesh counter electrode prevented acquisition of spectra during the anodization, so spectral analyses were performed after completion of the anodization.

PS was formed in electrolytes composed of either 4:5 (by volume) HPLC grade water:49 wt.% electronics grade HF (referred to hereafter as 29% HF in water) or 4:5 absolute ethanol:49 wt.% electronics grade HF (referred to hereafter as 29% HF in ethanol). The silicon wafers were electrolyzed at a current density of 30 mA/cm^2 for 13 minutes under room light. These conditions produce PS layers that are approximately 20 μm thick and 60-70% porous.

Spectroscopy was performed with a 457.9 nm argon ion laser focused to an approximately 1 x 0.1 mm area on the silicon sample. The laser power was about 100 mW, resulting in a power density of about 100 W/cm^2. PL and Raman spectra were measured with a scanning double monochromator and a photon-counting photomultiplier tube with a GaAs photocathode. The accuracy of the measurements was about ± 1 cm^{-1}, and the full width at half maximum resolution was about 6 cm^{-1}.

RESULTS

In Figure 1, the *ex situ* PL spectra taken from the edge and from the center of a silicon sample electrolyzed in 29 wt.% HF in ethanol are shown. The PL intensity for the PS near the edge of the wafer is much greater (note the scale factor) and shifted to longer wavelengths compared to the PL for PS at the center of the wafer. The four peaks in the spectra for the PS in the center of the wafer are possibly due to interference effects. Assuming a value of 1.4 for the refractive index of PS [13], the thickness of the layer producing the interference effects is calculated to be about 5 μm. This is less than the PS thickness calculated from gravimetric measurements (about 20 μm) and may reflect some laser-induced degradation of the PS film.

In Figure 2, the low frequency region of the Raman spectra for the same samples is shown, and the peaks due to the Si-Si vibrational mode of crystalline silicon are observed. Both peaks are shifted from the frequency at which the peak for bulk, crystalline silicon is observed (521 cm^{-1}, [9]), the peaks being observed at 515 cm^{-1} for the sample at the wafer center and at 507 cm^{-1} for the sample at the wafer edge. This is consistent with silicon crystallite sizes at the wafer center of about 4 nm and at the wafer edge of about 2.5 nm, based on the magnitude of the peak shift [9]. Both peaks are also much broader in the lower frequency portion of the spectrum than the crystalline silicon peak and have significant intensity at 480 cm^{-1} (the frequency corresponding to a peak observed in amorphous silicon), with the sample near the edge showing the greater effect.

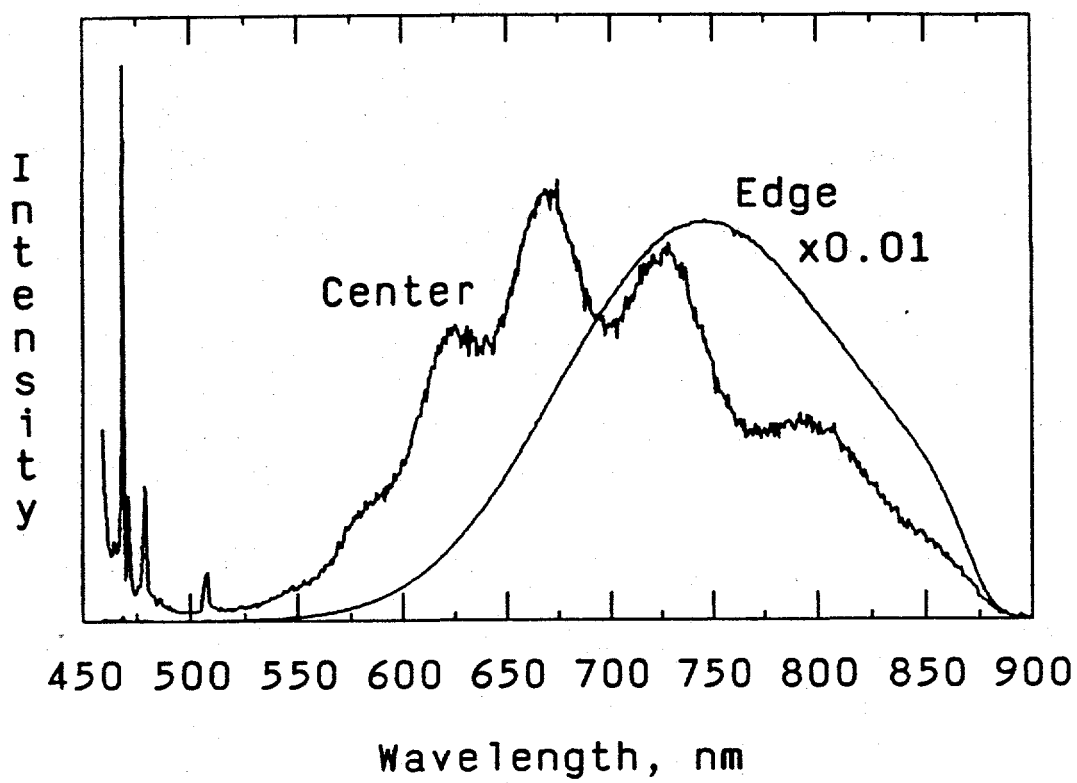

Figure 1. *Ex situ* PL spectrum of porous silicon sample (formed by electrolysis in 29% HF in ethanol) at center and edge of wafer. Spectra were recorded about 72 hours after electrolysis with the sample exposed to air during that interval. The narrow features between 457 nm and 510 nm are Si-Si and Si-H Raman bands.

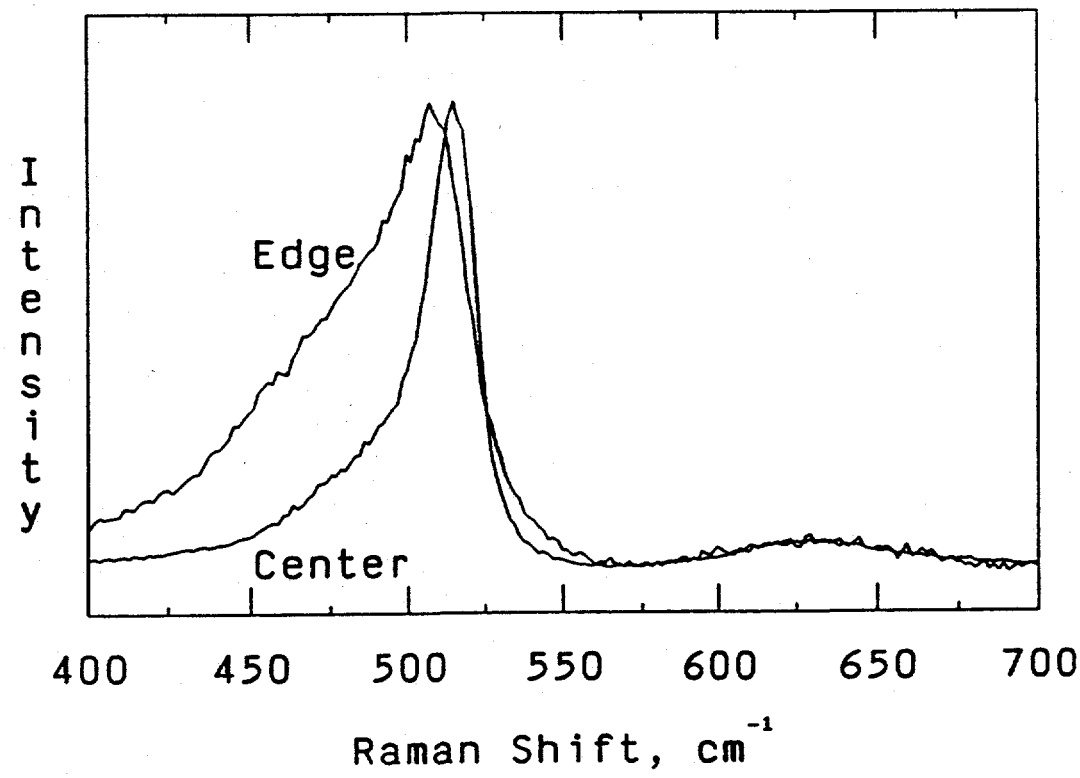

Figure 2. *Ex situ* Raman spectra of porous silicon sample (formed by electrolysis in 29% HF in ethanol) at center and edge of wafer. Spectra were recorded about 72 hours after electrolysis with the sample exposed to air during that interval. Peaks in spectra for center and edge of wafer are at 515 cm^{-1} and 507 cm^{-1}, respectively.

In Figure 3, the Si-H Raman region for the same samples is shown. Peaks due to the symmetric and asymmetric stretches of Si-H bonds are observed. There are no peaks observed in the vicinity of 2000 cm^{-1}, indicating there is no significant silicon monohydride (Si-H) concentration in the PS samples [14]. The PS at the wafer center shows 3 sharp peaks at 2090, 2112, and 2140 cm^{-1}, consistent with the presence of both SiH_2 and SiH_3 surface species on the PS [14]. It should be noted here that these peak assignments were made based on published work on the infrared and Raman spectra of SiH_4, Si_2H_6, and higher silanes [14]. Other workers [15] have identified the triplet at 2090, 2110, and 2140 cm^{-1} as Si monohydride, dihydride, and trihydride stretches, respectively. In either case, it is clear that the PS at the wafer center is hydrogen-passivated. In contrast, the spectra for the PS at the wafer edge shows very broad peaks shifted to higher frequencies, which is what would be expected for Si-H species that also have an electronegative atom (such as oxygen) bonded to the Si atom [16].

We interpret the differences observed in Figures 1-3 in terms of the non-uniformity in the current distribution in the electrolysis process. It can be shown that for the parameters used in this process (current density, electrode area, electrolyte resistivity), the current distribution will not be uniform across the diameter of the silicon wafer but instead will be higher at areas near the edge and lower near the center [17]. The higher current density will result in a thicker and/or more porous PS layer. Based on the results seen in Figures 1-3, we propose that the higher current density produced a more porous layer at the edge with smaller crystallites more susceptible to oxidation. This resulted in a PL red shift and 100-fold increase in intensity.

In separate experiments, we obtained *ex situ* PL spectra of 4 separate PS samples that were electrolyzed in 29% HF in water. The samples were allowed to soak in the electrolyte for various lengths of time (0-15 hours) before being removed for spectroscopic study. In all cases, the spectra were taken from a region near the center of the wafer. We observed a blue shift in the peak intensity of the PL spectrum for samples that were chemically etched by the HF electrolyte, in agreement with previous results [2]. This blue shift was accompanied by a shifting and broadening of the crystalline silicon Raman peak, a similar (but not nearly as dramatic) effect to that observed in Figure 2. In addition, the samples exposed to HF for longer time periods show a greater degree of oxidation in the Si-H portion of the Raman spectrum, similar to the effect seen in Figure 3.

The red shifted PL (from regions of higher current density, Figure 1) and the blue shift observed for the PS-in-HF chemical dissolution experiments described above are difficult to reconcile with the measured Raman spectra, as the trends observed in the Raman spectra are quite similar. It should be noted, however, that exposure of PS to O_2 at 200 °C (in the dark) or the exposure of PS to O_2 at room temperature under ultraviolet light reduces the efficiency of the PL, but also produces a red shift in the PL and replaces the infrared signal of Si-H bonds with that of O-Si-H bonds [18]. This surface oxidation also produces dramatic changes in the Raman spectra, namely a large broadening of the c-Si Raman peak and a shift to lower frequencies [10]. These results were interpreted as resulting from surface-induced disorder effects. Since our experiments were conducted in the presence of oxygen (i.e., in room air), we may be observing an effect of a similar nature. However, all our spectroscopic experiments were performed under identical conditions of laser power density and spectral acquisition times. Therefore, in order for this phenomenon to be the cause of the effects we observe, certain types of PS (e.g., PS at the edge of the wafer) would have to be more susceptible to surface-induced disorder effects than other types of PS (e.g., PS at the center of the wafer). This matter is presently under further investigation.

In Figure 4, the PL spectra for one PS sample is shown at 2 different times following electrolysis in 29% HF in ethanol. The spectra have been normalized by scaling to the height of the crystalline silicon Raman peak at ca. 521 cm^{-1}. The *in situ* spectrum, recorded 15 minutes following electrolysis, shows very little luminescence above background except in the 825-875 nm region, where a small peak is observed. Since the photomultiplier tube used in this study has very little sensitivity above 875 nm, it is possible that the peak observed in this PL spectrum is an artifact and that the actual peak in the PL spectrum is well above 900 nm. After this spectrum was recorded, the PS sample was removed, rinsed with HPLC grade water, and dried. The *ex situ* spectrum shows a large blue shift as well as a significant increase in intensity

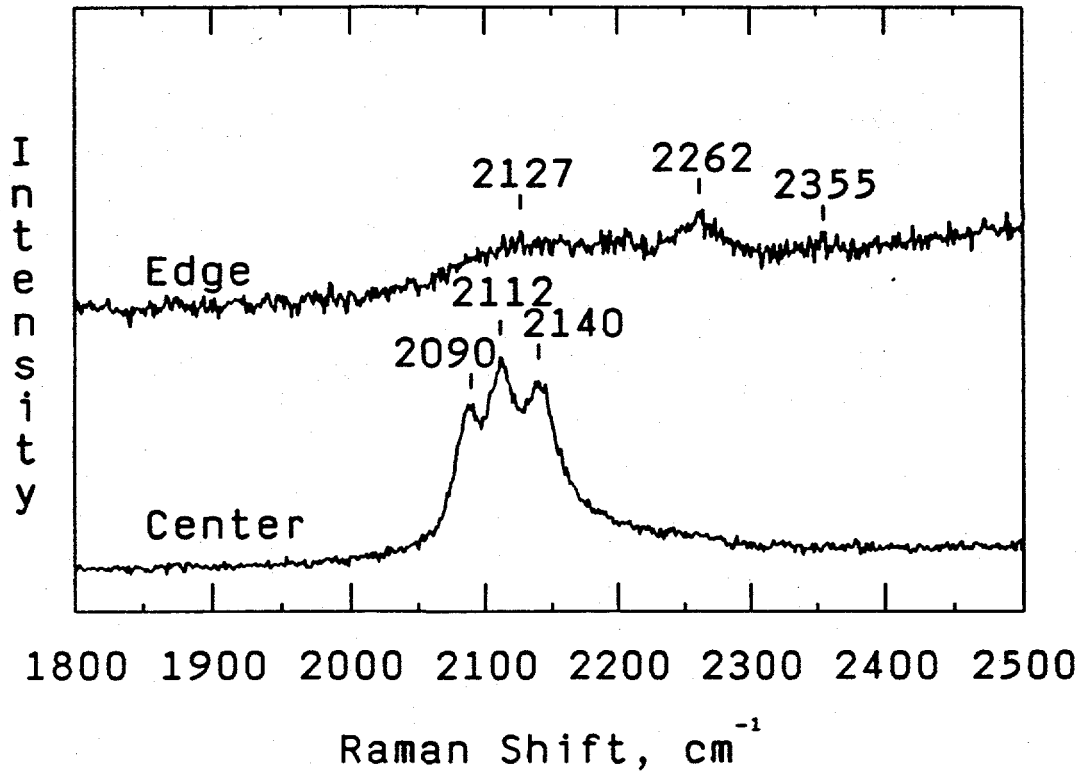

Figure 3. *Ex situ* Raman spectra of porous silicon sample (formed by electrolysis in 29% HF in ethanol) at center and edge of wafer. Spectra were recorded about 72 hours after electrolysis with the sample exposed to air during that interval.

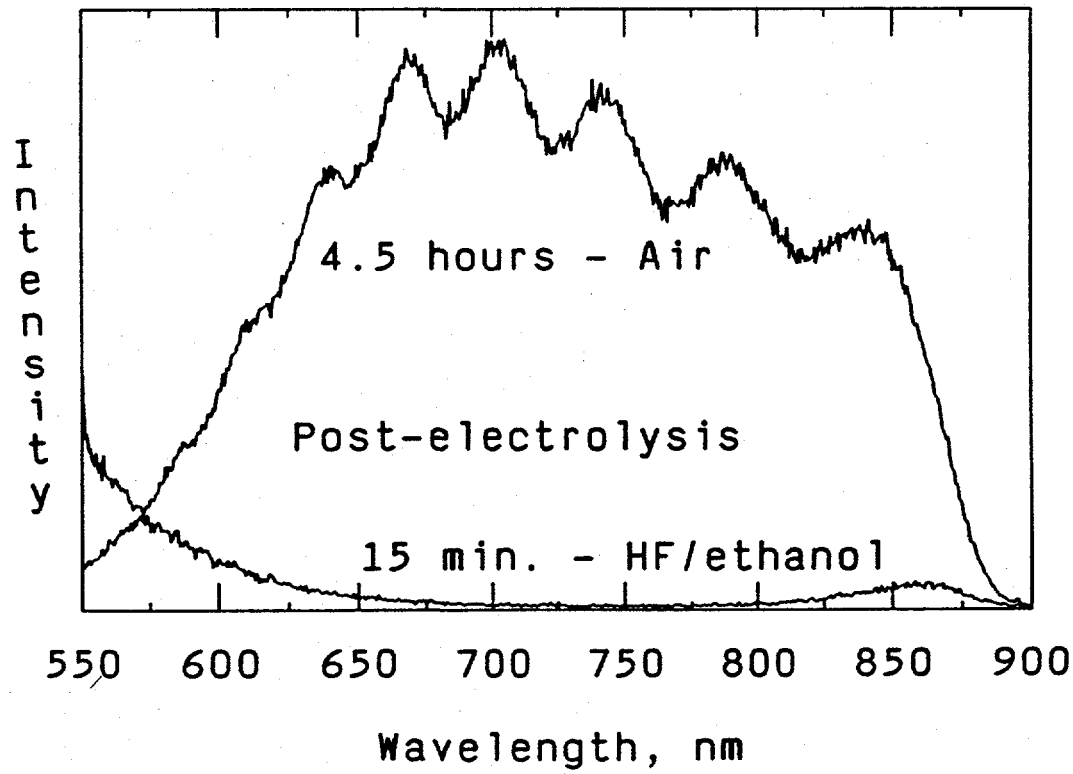

Figure 4. *In situ* PL spectrum (recorded 15 minutes after electrolysis) and *ex situ* PL spectrum (recorded 4.5 hours after electrolysis) of porous silicon formed by electrolysis in 29% HF in ethanol. Spectra are scaled to the height of the crystalline Si Raman peak at ca. 521 cm^{-1}.

compared to the *in situ* spectrum. In addition, the interference fringes described earlier are observed again. A possible cause for the low quantum efficiency observed in the *in situ* experiment is photochemical etching of the PS in the hydrofluoric acid electrolyte.

In another *in situ* experiment, we immersed air-exposed PS in water and observed a 15-fold increase in PL intensity along with a blue shift in the luminescence maximum compared to the spectrum obtained in air. Here, photochemical etching of PS is not expected to be a factor. Then, replacement of the water with 29% HF in ethanol resulted in a dramatic quenching of the PL, similar to the result in Figure 4. Further *in situ* experiments will be performed by replacing the HF electrolyte with water or other solutions where photochemical etching does not occur (e.g., HCl) to attempt to further understand the correlation between Raman and PL spectra and their impact on the proposed mechanisms for visible light emission from PS. The special spectroelectrochemical cell described in this paper, along with the techniques we have developed for performing *in situ* Raman and PL spectroscopic measurements, will allow us to obtain reliable correlations between the presence of chemical species in the PS and the energy and intensity of the photoluminescence.

ACKNOWLEDGMENTS

The authors gratefully acknowledge the assistance of R. L. Simpson with the spectroscopic measurements. This work performed at Sandia National Laboratories supported by the U.S. Department of Energy under contract number DE-AC04-076DP00789.

REFERENCES

1. A. Gee, J. Electrochem. Soc., 107, 787 (1960).
2. L. T. Canham, Appl. Phys. Lett., 57, 1046 (1990).
3. A. G. Cullis and L. T. Canham, Nature, 353, 335 (1991).
4. M. S. Brandt, H. D. Fuchs, M. Stutzmann, J. Weber, and M. Cardona, Sol. St. Comm., 81, 307 (1992).
5. C. Tsai, K.-H. Li, D. S. Kinosky, R.-Z. Qian, T.-C. Hsu, J. T. Irby, S. K. Banerjee, A. F. Tasch, J. C. Campbell, B. K. Hance, and J. M. White, Appl. Phys. Lett., 60, 1700 (1992).
6. R. P. Vasquez, R. W. Fathauer, T. George, A. Ksendzov, and T. L. Lin, Appl. Phys. Lett., 60, 1004 (1992).
7. Y. H. Xie, W. L. Wilson, F. M. Ross, J. A. Mucha, E. A. Fitzgerald, J. M. Macaulay, and T. D. Harris, J. Appl. Phys., 71, 2403 (1992).
8. M. B. Robinson, A. C. Dillon, D. R. Haynes, and S. M. George, Appl. Phys. Lett., 61, 1414 (1992).
9. Z. Sui, P. P. Leong, I. P. Herman, G. S. Higashi, and H. Temkin, Appl. Phys. Lett., 60, 2086 (1992).
10. J. C. Tsang, M. A. Tischler, and R. T. Collins, Appl. Phys. Lett., 60, 2279 (1992).
11. R. Tsu, H. Shen, and M. Dutta, Appl. Phys. Lett., 60, 112 (1992).
12. F. H. Pollak, Test and Measurement World, 5, 2 (1985).
13. G. W. 't Hooft, Y. A. R. R. Kessener, G. L. J. A. Rikken, and A. H. J. Venhuizen, Appl. Phys. Lett. 61, 2344 (1992).
14. M. H. Brodsky, M. Cardona, and J. J. Cuomo, Phys. Rev. B., 16, 3556 (1977).
15. Y. J. Chabal, G. S. Higashi, K. Raghavachari, and V. A. Burrows, J. Vac. Sci. Technol. A, 7, 2104 (1989).
16. G. Lucovsky, R. J. Nemanich, and J. C. Knights, Phys. Rev. B., 19, 2064 (1979).
17. C. Wagner in Advances in Electrochemistry and Electrochemical Engineering, edited by C. Tobias and P. Delahay, (Elsevier Science Publishers, New York, 1962), 2, pp. 1-14.
18. M. A. Tischler, R. T. Collins, J. H. Stathis, and J. C. Tsang, Appl. Phys. Lett., 60, 639 (1992).

Appendix VI. "Photoluminescence of Silicon Nanostructures Formed by Ion Implantation"

PHOTOLUMINESCENCE OF SILICON NANOSTRUCTURES FORMED BY ION BEAM IMPLANTATION

D. A. REDMAN, D. M. FOLLSTAEDT, T. GUILINGER, AND M. KELLY
Sandia National Laboratories, Albuquerque, NM.

ABSTRACT

A new method was used to fabricate nanometer-scale structures in Si for photoluminescence (PL) studies. He ions were implanted to form a dense subsurface layer of small cavities (1-8 nm diameters). The implanted specimens were either annealed in H or anodized with HF to evaluate the quantum confinement model for PL from porous Si. Incomplete passivation apparently prevented PL in the H-annealed specimens. Implantation combined with anodization produced a substantial blue shift relative to anodization alone, which is consistent with quantum confinement.

INTRODUCTION

Recent reports of light emission from electrochemically etched porous silicon[1] have suggested the possibility of silicon-based optoelectronic devices compatible with current VLSI processing technology. This has stimulated extensive research to identify the physical mechanisms responsible for the observed visible luminescence. The mechanisms suggested to date include (1) quantum-size effects[1], (2) surface-bound, wide bandgap siloxene-like polymers[2], (3) hydrogenated amorphous silicon,[3,4] and (4) dihydride bonds on the Si surfaces[5]. The wet chemical methods for producing porous silicon involve an aqueous HF electrolyte and necessarily expose the porous material to fluorine, hydrogen, and oxygen. Furthermore, a native oxide covers the exposed surfaces when the specimen is removed from the electrolyte. The simultaneous presence of all the elements required for each mechanism precludes independent evaluation of the proposed models. We have formed nanometer-size structures ("nanostructures") in silicon using helium ion implantation to produce a dense, subsurface layer of bubbles[6,7]. Implantation creates a porous layer which is free from contamination and is removed from any oxidizing ambient. The nanostructure dimensions are similar to the pore diameters observed in electrochemically produced porous silicon. We have examined specimens prepared with a range of He fluences and annealing atmospheres for photoluminescence in an effort to address independently the quantum size and surface hydride models for light emission.

SPECIMEN PREPARATION AND CHARACTERIZATION

Specimens were prepared by ion implanting high-purity (001) Si with He^+ at 30 keV to fluences of 1.0 to 4.2×10^{17} He/cm^2. Some specimens were annealed at 700 or 800°C in vacuums of $\leq 10^{-7}$ torr to coarsen the cavities. Specimens were then "soaked" in 650 torr of H_2 or D_2 gas at 600°C for up to 88 hours to passivate the cavity surfaces and lattice defects by diffusion of D or H to the cavity layer, where it bonds to Si atoms on the cavity surfaces.[8] Specimen microstructures were examined in [110] cross-section orientation by transmission electron microscopy (TEM) at 200 kV. Specimens were prepared by gluing two pieces together at their implanted surfaces. The materials were mechanically polished ("dimpled") at the glue line until transparent to orange light, and ion milled to produce a hole with thin edges near the glue line.[9]

Mat. Res. Soc. Symp. Proc. Vol. 279. ©1993 Materials Research Society

The microstructure of a specimen just after implantation of $1.0x10^{17}$ He/cm^2 is shown in Figure 1a. There is a subsurface layer which appears darker due to lattice damage. The specimen was tilted off the [110] zone axis in order to reduce diffraction contrast and imaged in an underfocussed condition (-1.5 μm) to enhance the contrast of the cavity edges by Fresnel fringes. In this figure, the cavities are so small that they appear as white spots with a black circle around them. Their density is so high that it is difficult to avoid overlapping cavity images, but for this lowest fluence their size is seen to be 1-2 nm in diameter. The area most dense with cavities is consistent with the projected range of R_p = 0.29 μm and with the width ΔR_p = 0.09μm predicted by the TRIM90 simulation program[10]. In this condition, the cavities are filled with He and are termed "bubbles". They probably still contain He after soaking in H at 600°C. The 600°C treatment may have enlarged them somewhat, but probably to no more than 7 nm as observed for 700°C anneals[6].

For specimens annealed at 700 or 800°C, a well-defined subsurface layer of cavities is found between 0.15 -0.35 μm. These anneals cause the He to diffuse from the cavities and out the surface of the specimen[6]. The cavities are larger and can be individually identified for counting and sizing to obtain the cavity volume within the layer[7]. The average of the depth-integrated volume in the layer for these two temperatures is 14 $\pm$ 4 nm^3/nm^2, which gives a porosity of 7%.

Room temperature Fourier transform infrared spectroscopy (FTIR) measurements of specimens implanted with $1.0x10^{17}$ He/cm^2 and annealed at 700 or 800°C have been carried out in conjunction with TEM for analysis of the cavity structure following annealing in H_2[11]. Strong absorption was detected near the surface Si-H stretch mode frequencies of 2089 and 2100 cm^{-1}. The presence of the dihydride scissors mode near 900 cm^{-1} could not be determined.

Increasing the He fluence increases the bubble size and is expected to increase the porosity. Figure 1b shows the microstructure found after implanting the highest fluence of $4.2x10^{17}$ He/cm^2. The isolated circular cavities have increased in size to 3-8 nm in diameter, but near the center of the layer, the cavities are seen to have agglomerated into elongated voids which extend up to ~60 nm parallel to the surface and may be interconnected. A porosity of 29% is predicted for this fluence by scaling the low-fluence results. Other specimens show cracks extending farther. In this area of the specimen the implanted layer was still intact, and electron diffraction (Figure 1c) could be used to examine the region with the highest cavity density. The pattern shows no evidence of diffuse rings that would indicate that amorphous Si had been formed by the ion irradiation damage. We also examined such patterns for evidence of a "bubble lattice" as seen in metals implanted with high fluences of He[12]. Some diffuse scattering is seen about the central spot, but neither rings nor spots indicative of a non-random spatial arrangement of the bubbles or long-range ordering of their positions were found.

Cracks in the layer and blistering of the surface were most pronounced for $2.6x10^{17}$ He/cm^2. Figure 1d is an optical micrograph of the implanted surface showing areas in which much of the surface layer has broken away. In the brighter areas where the layer still remains, circular holes are seen where blisters have broken open; a few domes of unbroken blisters can be also be seen. High pressures are expected for He in the cavities, which places the layer in compressive stress. As the porosity increases the subsurface material strength is reduced, which leads to the blistering. Although this specimen is predicted to have lower porosity (18%), it had more surface damage than $4.2x10^{17}$ He/cm^2, and TEM showed larger, interconnected cracks. A specimen with $1.6x10^{17}$ He/cm^2 showed no cracking within the layer and no surface blistering.

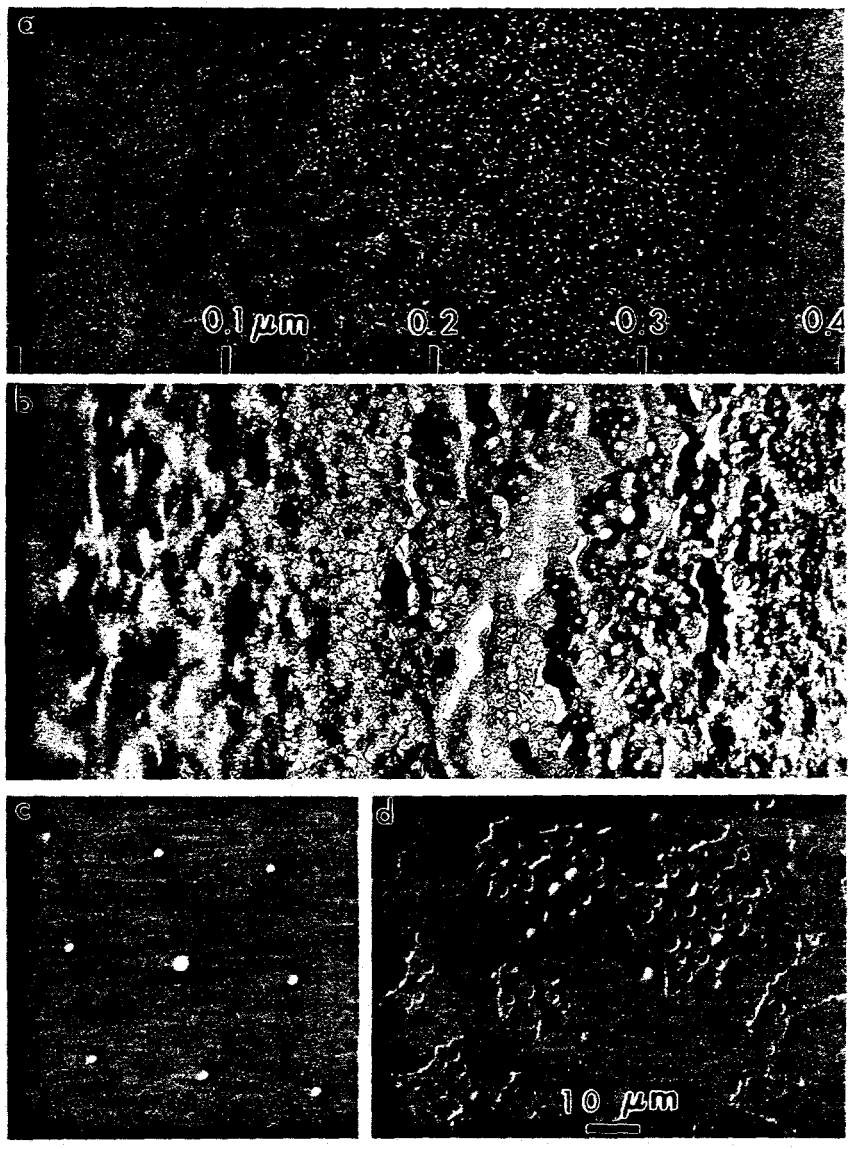

Figure 1. a) [110] cross-section TEM bright-field image of (001) Si implanted with 1.0×10^{17} He/cm^2 at 30 keV, imaged at -1.5 μm defocus. b) Equivalent image to a) but with 4.2×10^{17} He/cm^2, imaged at -0.5 μm defocus. c) Electron diffraction pattern from region of high cavity density in b). d) Nomarski optical micrograph of the surface of a specimen implanted with 2.6×10^{17} He/cm^2 at 30 keV.

Photoluminescence measurements were made at room temperature for both as-implanted and implanted/annealed specimens, both before and after H_2 soaking. Spectra were taken using a 0.22 m double monochromator (SPEX 1680B) employing 1200 gr/mm gratings blazed at 500 nm. Slit widths were typically 100 - 500 μm. A cooled GaAs photocathode PMT was used in both a synchronous (lock-in) detection mode and a photon counting mode with a RMS dark noise of less than one count. An argon laser operating at 457 nm was used for excitation at power densities less than 10 W/cm^2.

PHOTOLUMINESCENCE RESULTS AND DISCUSSION

Figure 2 compares the photoluminescence spectrum from an implanted specimen to that from electrochemically prepared porous silicon on a <100>, 1 Ω-cm, p-type wafer. Anodization was done in a Pt-grid "double cell" with a 5% HF solution at a current density of 0.55 mA/cm^2 for 765 seconds. The electrochemically produced specimen was 73% porous, as determined by gravimetric measurements. The implanted specimen received 1.0x10^{17} He/cm^2 at 30 keV with no subsequent annealing prior to D_2 soaking at 600°C. The porous specimen yields a strong photoluminescence band extending from 550 nm to 850 nm and centered at 700 nm. The dip seen in the trace is a spectrometer artifact. The implanted specimen shows no evidence of photoluminescence over a similar band. Transmission through a 0.35 μm silicon overlayer is ~93% at 700 nm thus absorption of any emitted light by this overlayer is not a factor. The numerous dislocations in the implanted layer may provide nonradiative recombination centers which quench any photoluminescence if the D_2 soak did not passivate them sufficiently.

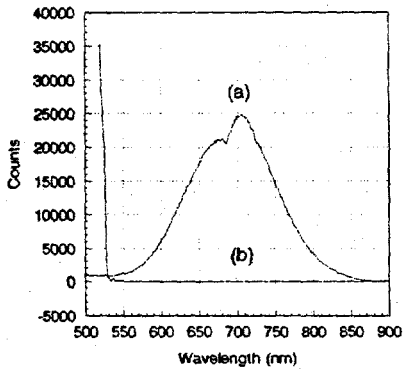

Figure 2. Curve (a) shows PL spectrum of 73%, 0.35μm thick porous silicon. Curve (b) shows PL spectrum of specimen implanted with 1x10^{17} He/cm^2.

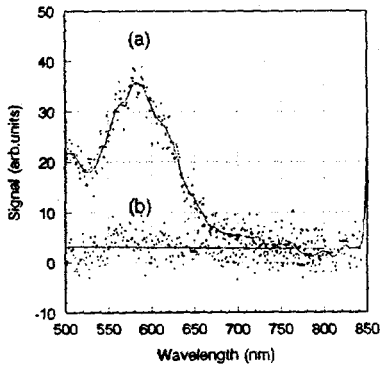

Figure 3. Curve (a) shows PL spectrum of a 73%, 0.35 μm thick porous region grown on an implanted (1x10^{17} He/cm^2) substrate while curve (b) shows the spectrum obtained from the substrate alone.

Specimens prepared with the different implantation fluences and annealing conditions discussed above all gave spectra similar to the lower trace of Figure 2. Specimens implanted with $1.0x10^{17}$ He/cm^2 were annealed in vacuum at 700 or 800°C to reduce implantation-induced nonradiative recombination centers. These specimens were examined before and after subsequent soaks in H aimed at passivating defects as well as terminating the cavity surfaces with H.[8] Neither annealing condition yielded measurable photoluminescence.

We have also examined the effect of a He-implanted layer on the electrochemical formation of porous silicon and its photoluminescence. The wafer was implanted with $1x10^{17}$ He/cm^2 and was subsequently anodized over 15% of its area. The anodization conditions used produced a 73% porous layer with a depth of 0.3 μm like that examined in Figure 2. Thus it is expected that the porous region extends into the implanted layer, which can affect its etch rate and final porosity. Figure 3 shows the photoluminescence spectrum from this specimen. The upper trace was recorded with the excitation incident on the porous region. The lower trace shows the spectrum recorded under identical conditions with the excitation incident on the implanted substrate alone. The dominant features of the upper trace are the PL band peaking at 550 nm on top of an exponential tail sloping away from the excitation line. The presence of this tail in the porous Si spectrum alone indicates that the anodization enhances the surface scatter of the excitation light to a level that is not rejected by the spectrometer. The effect of increasing the porosity of electrochemically produced porous silicon is to shift the peak of the PL band to shorter wavelengths. When the exponential tail is subtracted off the upper trace, there is a 120 nm blue shift of the PL peak from that of the 73% porous specimen shown in Figure 2. This indicates that the local porosity is very high in the porous/implanted region. This is consistent with the anodic reaction rate increasing when the implanted layer is reached, effectively shrinking the crystalline silicon domains between the nanocavities as shown schematically in Figure 4. The smaller domain sizes in turn lead to the observed blue shift.

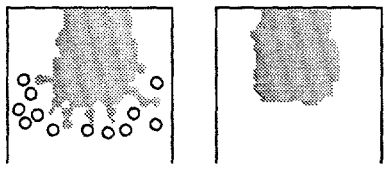

Implanted Unimplanted

Figure 4. Model for porous silicon formation on He implanted substrate.

CONCLUSIONS

None of our implantation conditions have yielded photoluminescence thus far. This may be due to the presence of non-radiative recombination centers. We attempted to passivate defects and dangling bonds on the surfaces of the cavities by soaking in D_2 or H_2. Examination of such treatment with FTIR shows that monohydride (Si-H) bonds form on the cavity interiors, but to date, dihydride (Si-2H) bonds have not been detected.[11] Our result is consistent with the finding that dihydride bonds are necessary for photoluminescence[13], but it does not confirm or dispell any of the models.

We were successful in altering the spectrum of electrochemically prepared porous Si by implanting He before anodization. The resulting blue shift is consistent with the quantum confinement model since the cavities are expected to increase the final porosity, but is not compelling.

In conclusion, we have used He ion implantation to create a dense layer of nanocavities in silicon. We have tailored their size and shape by varying annealing times and temperatures. Hydrogen has been introduced in a relatively controlled fashion to produce monohydride terminations of the interior surfaces. Ion implantation is a technologically attractive alternative for producing silicon nanostructures without the contamination unavoidable in wet chemical methods. However, lattice damage produced during implantation may limit its usefulness as an effective means of producing efficient photoluminescence from silicon. Although the presence of nonradiative recombination centers in our specimens prevents a firm conclusion concerning the validity of the quantum confinement model, the blue shift observed from a porous layer grown on an implanted substrate is consistent with it.

ACKNOWLEDGMENTS

The authors thank M. P. Moran for preparing cross-section TEM specimens and D. M. Bishop for performing the ion implantations and the anneals. Discussions with S. M. Myers, W. R. Wampler and H. J. Stein were quite valuable. This work performed under the auspices of the U. S. Department of Energy under contract DE-AC04-76DP00789.

REFERENCES

1. L. T. Canham, Appl. Phys. Lett. **57**, 1046 (1990).
2. H. D. Fuchs, M. S. Brandt, M. Stutzmann and J. Weber, Mat. Res. Soc. Symp. Proc. **256**, 159 (1992).
3. K. H. Jung, S. Shih, T. Y. Hsieh, J. C. Campbell, D. L. Kwong, T. George, T. L. Lin, H. Y. Liu, J. Zavada and S. Novak, Mat. Res. Soc. Symp. Proc. **256**, 31 (1992).
4. R. W. Fathauer, T. George, A. Ksendzov, T. L. Lin, W. T. Pike, R. P. Vasquez and Z.-C. Wu, Mat. Res. Soc. Symp. Proc. **256**, 165 (1992).
5. S. M. Prokes, O. J. Glembocki, V. M. Bermudez, R. Kaplan, L. E. Friedersdorf and P. C. Searson, Mat. Res. Soc. Symp. Proc. **256**, 107 (1992).
6. A. Van Veen, C. C. Griffioen and J. H. Evans, Mat. Res. Soc. Symp. Proc. **107**, 449 (1988); C. C. Griffioen, J. H. Evans, P. C. DeJong and A. Van Veen, Nucl. Inst. Meth. **B27**, 417 (1987).
7. D. M. Follstaedt, S. M. Myers and H. J. Stein, Mat. Res. Soc. Symp. Proc. **279** (elsewhere herein) (1993).
8. W. R. Wampler, S. M. Myers and D. M. Follstaedt, submitted to Physical Review B.
9. D. M. Follstaedt, S. M. Myers, W. R. Wampler, and H. J. Stein, Proc. 50th Ann. Mtg. Electron Microscopy Society of America (San Francisco Press, 1992), p. 334.
10. J. F. Ziegler, J. P. Biersack and U. Littmark, The Stopping and Range of Ions in Solids, (Pergamon Press, New York, 1985); J. F. Ziegler, private communication, 1990.
11. H. J. Stein, S. M. Myers and D. M. Follstaedt, Journal of Applied Physics, in press.
12. D. J. Mazey and J. H. Evans, J. Nucl. Mat. **138**, 16 (1986).
13. C. Tsai, K.-H. Li, J. Sarathy, S. Shih, J. C. Campbell, B. K. Hance and J. M. White, Appl.Phys. Lett. **59**, 2814 (1991).

Appendix VII. "Control of Photoluminescence from Porous Silicon"

Nanotechnology 3 (1992) 202–204. Printed in the UK

Control of photoluminescence from porous silicon

J C Barbour, D Dimos, T R Guilinger and M J Kelly

Sandia National Laboratories, Albuquerque, NM 87185, USA

Received 12 June 1992, accepted for publication 25 November 1992

Abstract. A description of ion-irradiation-induced reduction in the photoluminescence (PL) signal from porous silicon is given and a simple model which is consistent with a nanocrystalline Si structure is presented. Ion irradiation with 250 keV Ne is used to controllably reduce the integrated PL signal by 20% after a fluence of 4×10^{12} Ne cm^{-2} and completely eliminate the PL signal after a fluence of 4×10^{13} Ne cm^{-2}. The use of vacuum and air annealing to recover ion-induced damage is also described, but the high temperatures for annealing cause elimination of the PL signal.

1. Introduction

Visible light emission from silicon has recently been thought to be negligible. Although hydrogenated amorphous Si [1] and polysilane-based alloys [2] had been known to emit light, crystalline Si has an indirect bandgap which allows only for phonon-assisted radiative bandgap transitions which are highly inefficient and produce light outside the visible range ($\simeq$ 400–800 nm). Current work on porous Si [3] and thin films of Si [4] microcrystallites (2–5 nm diameter) have demonstrated photoluminescence (PL) from infrared to green. In order to make this new physical phenomenon compatible with conventional integrated circuit technology, a method is needed to control and pattern light-emitting regions of this Si-based material. This paper will demonstrate the use of ion irradiation to controllably reduce the emission of red light from porous silicon. In addition, the behaviour of the PL intensity at room temperature as a function of incident-light energy and intensity will be examined. Finally, the effects on PL of annealing treatments to recover ion-beam damage will be discussed.

2. Experimental details

The samples were made from (100)-oriented, 1 Ω cm resistivity, boron-doped, p-type silicon. The porous silicon (PS) layer was formed using a double-tank electrochemical cell containing 5 wt.% HF in H_2O and using a 0.5 mA cm^{-2} anodization current density. The PS layer was 290 nm thick with a porosity of 73%. Elastic recoil detection (ERD) with a 24 MeV Cl^{+5} beam was used for composition analysis of light elements (Z = 1–9) in the PS layer. Figure 1 shows an ERD spectrum collected for an incident fluence of 5.6×10^{14} Cl cm^{-2}. The angle of incidence for the analysis beam was 75° from the sample normal and the scattering angle was 30°. A 6 μm mylar foil was used to decrease the signal of scattered Cl reaching the detector. However, some Cl penetrated the foil and added a background signal below the H signal. This background has been subtracted from the spectrum in figure 1. The peaks in the ERD spectrum appear as bell-shaped curves (poor depth resolution) because the porous nature of the sample limits the depth resolution. For this reason, the following analysis uses integrated peaks to give areal densities (atoms cm^{-2}) for the entire 290 nm thick layer rather than a concentration depth profile. In addition to Si (3.9×10^{17} Si cm^{-2}, taking into account the reduced density due to the high porosity), the PS layer contains 20 at/% O (8×10^{16} O cm^{-2}), 4 at.% H (1×10^{16} H cm^{-2}), and 2 at.% C. This amount of oxygen is much less than that needed to completely oxidize the PS layer and is approximately equal to the amount expected for a 1 nm thick native oxide covering the surface area.

An Ar laser was used as a PL excitation source: 514.5 nm, 496 nm, 476 nm and 457 nm. The light was incident at an angle of 60° from the sample normal which yields a light penetration depth of $\simeq$ 0.5 m for these wavelengths in bulk Si, and the power density for each wavelength was varied from 35 mW cm^{-2} to 685 mW cm^{-2}. The emitted PL light was passed through a spectrometer containing a 150 lines mm^{-1} grating and then collected with a CCD area-array photodetector. The resolution of this detection system was $\simeq$ 2 nm.

Portions of the sample were irradiated with 250 keV Ne^+ at an angle of incidence of 5° from the surface normal for fluences from 4×10^{12} Ne cm^{-2} (0.0008 dpa) to 4×10^{14} Ne cm^{-2} (0.08 dpa). A damage level of 0.8 dpa or greater is needed to amorphize Si at room

0957-4484/92/040202+03$07.50

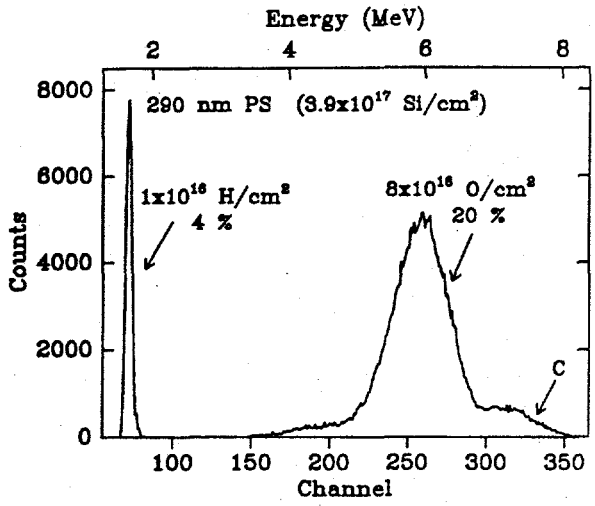

Figure 1. 24 MeV Cl^{+5} elastic recoil detection (ERD) was used to measure the content of H, O and C in the 290 nm thick porous silicon (PS) layer. The density of the PS layer was taken as 27% of bulk Si which yields 3.9 × 10^{17} Si cm^{-2} in this layer. (2% C corresponds to 8 × 10^{15} C cm^{-2}).

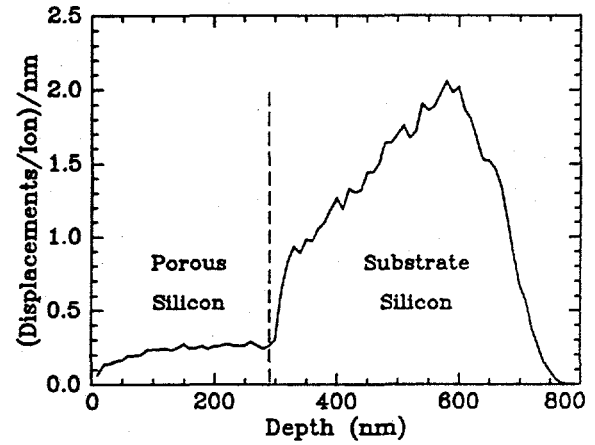

Figure 2. The displacement profile from a TRIM [5] calculation of 250 keV Ne irradiation of a 73% porous Si layer on an Si substrate. A displacement energy of 15 eV was used for this calculation.

temperature. The range of these ions and the level of damage was determined from a TRIM [5] Monte Carlo simulation using a displacement energy of 15 eV displacement $^{-1}$. The range of 250 keV Ne was approximately 600 nm, as shown in figure 2, and the level of damage in the less dense PS layer was approximately constant at 0.25 displacements ion^{-1} nm^{-1} throughout the layer.

3. Results

3.1. Unirradiated sample

The PL spectrum from the unirradiated area is shown as the solid line in figure 3. This figure shows a broad spectrum which is consistent with both line broadening due to finite particle size and to broadening due to a distribution of particle sizes. The PS layer emitted

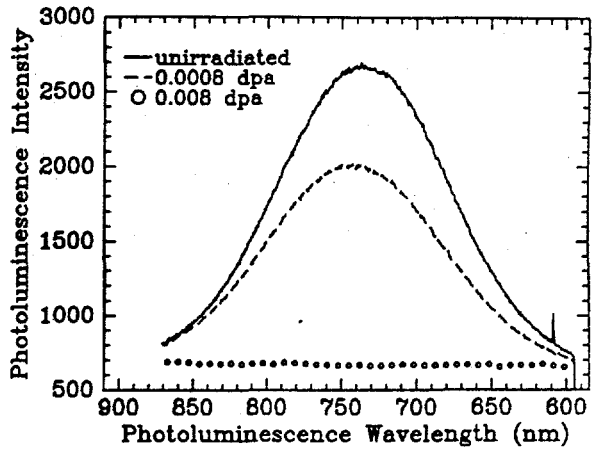

Figure 3. Photoluminescence intensity from the sample irradiated with 250 keV Ne to different fluence (damage) levels. A damage level of 0.0008 dpa corresponds to a fluence of 4 × 10^{12} Ne cm^{-2}.

light with a peak wavelength of 740 nm and this peak position showed little dependence on the excitation-light wavelength. The integrated photoluminescence intensity at room temperature increased linearly with excitation-light power density up to a saturation level. This result is consistent with an increase in the number of emitted photons being directly proportional to an increase in the number of excitation photons, up to a saturation level which corresponds to a saturation in the number of excited carriers. At a fixed power density below saturation, the ratio of the integrated photoluminescence intensities for 514 nm and 457 nm excitation wavelengths was 1.9–2.0 which is approximately equal to the ratio of the relative absorption coefficients in bulk crystalline Si. Thus, these results are consistent with the proposed model [3, 4] for luminescence from nanocrystalline silicon.

3.2. Irradiated samples

The red-light PL signal was controllably reduced by the use of 250 keV Ne ion irradiation to a damage level of 0.0008 dpa and completely eliminated above 0.008 dpa (figure 3, bottom curve). Ion-irradiation-patterned rectangular areas showed decreasing intensities of PL under Ar-laser light excitation, whereas the surrounding unirradiated areas remained at the same level of integrated intensity. The area irradiated to a damage level of 0.0008 dpa had an integrated intensity which was reduced from the unirradiated intensity by 20%.

The role of compositional changes during irradiation may be a significant mechanism in the reduction of PL efficiency. Therefore, the ERD signal was monitored as a function of fluence to determine if the H or O compositions changed during ion irradiation with 24 MeV Cl^{+5}. The H and O compositions remained approximately constant during the ERD data collection from a fluence of 5.6 × 10^{13} Cl cm^{-2} to 5.6 × 10^{14} Cl cm^{-2}. The smallest fluence which yielded enough statistics for ERD analysis was 5.6 × 10^{13} Cl cm^{-2} (1/10 of the fluence for the spectrum shown in figure 1) which corresponds

to a damage level of approximately 0.008 dpa [6]. This level of damage also completely eliminates the PL signal as shown in figure 3. This analysis suggests that H and O compositions are not significantly altered during irradiation; however, further work is necessary to non-destructively measure the H and O content of the samples for very low fluence irradiations.

The fact that the sample irradiated to a damage level of 0.0008 dpa had an integrated intensity which was reduced from the unirradiated intensity by 20% can be interpreted in terms of a simple physical model. If the mechanism causing the luminescence is due to quantum confinement in nanocrystalline boxes, then creating displaced atom(s) in these boxes would leave centers for rapid carrier recombination. The longer radiative recombination process would be eliminated for those boxes which were significantly damaged. An average box size of 1.7 nm sides has approximately 30 unit cells per box with eight Si atoms per unit cell. Therefore, a damage level of 0.0008 dpa corresponds to one displaced Si atom per five boxes of side 1.7 nm. This suggests that very few atoms need to be displaced in a given box (possibly as few as one displacement) in order to eliminate the PL from that box. This model describes the radiation sensitivity of the PS layer in terms consistent with a nanocrystalline structure, but the high radiation sensitivity is not exclusive to a crystalline material and is not meant to demonstrate the validity of that model. Similar descriptions could also have been developed for polysilane chains or amorphous Si:H. Instead, figure 3 demonstrates the high sensitivity of the PS material and the feasibility of using conventional integrated circuit technology (keV ion implantation) for controlling the emission of light from porous silicon. This result is important to PS processing because the current alternative is to pattern the Si wafer first and form the PS regions only in these patterned areas. Ion irradiation allows for the mass production of entire wafers of uniform PS which can be patterned with the ion beam, without subsequent chemical processing.

Figure 3 also demonstrates a secondary effect of ion irradiation on the luminescence. The PL peak from the irradiated sample is shifted to slightly higher wavelength (by $\sim$ 7 nm) and the full width at half-maximum of the peak from the irradiated sample is slightly larger than that of the unirradiated sample. As stated above, the wide breadth of the PL signal is consistent with both crystalline size effects and to a distribution of crystallite sizes. Although we expect fewer of the large crystallites (which would produce longer-wavelength luminescence), the larger crystallites have a larger cross-section for irradiation damage and we expected to observe a PL peak shift to smaller wavelengths and a narrowing of the PL spectrum based upon the model given above with a uniform distribution of damage in depth. This discrepancy indicates that secondary effects need further consideration in a more detailed model of ion-irradiation effects, e.g. strain effects or irradiation-induced strain relief effects on the PL properties.

4. Annealing

Finally, ion-implantation damage in crystalline Si has been studied extensively and the typical temperatures required to anneal out the damage are 600 °C or higher. Therefore, the irradiated samples (along with an unirradiated control sample) were vacuum annealed (10^{-7} Torr) at 650 °C for 30 min and the PL intensity was again measured. All samples, including the unirradiated control sample, showed complete loss of PL. A series of air annealing treatments were then done from 500 °C to 650 °C, and a sharp transition in the PL behaviour was found between 550 °C and 600 °C. Anneals for 15 min at 500 °C and 550 °C caused the PL intensity to decrease but the red light was still visible, whereas anneals for 1 min and 15 min at 600 °C both caused elimination of the PL signal. Further work must be done to determine the cause of the luminescence loss with annealing, but again the possible mechanisms which are known to occur in Si at these temperatures are (1) structural changes such as strain relaxation or relaxation of amorphous silicon, and (2) compositional changes such as the loss of H or O (which may be critical in passivating surfaces and defects for increased carrier lifetimes).

5. Summary

Red-light photoluminescence from a porous silicon layer was controllably reduced by the use of ion irradiation to a damage level of 0.0008 dpa and eliminated by ion irradiation at and above a level of 0.008 dpa. Ar-laser light excitation caused the porous silicon layer to emit light at a peak wavelength of 740 nm, independent of the excitation-light wavelength. Below saturation, the integrated photoluminescence intensity at room temperature increased linearly with excitation-light power density. At a fixed power density below saturation, the ratio of the integrated photoluminescence intensities for 514 nm and 457 nm excitation wavelengths was 1.9–2.0 which is approximately equal to the ratio of the relative absorption coefficients in bulk Si.

Acknowledgments

This work was supported by the US DOE Office of Basic Energy Sciences under contract DE-AC04-76DP00789.

References

[1] Wolford D J, Reimer J A and Scott B A 1983 *Appl. Phys. Lett.* **42** 369
[2] Kagawa T, Fujino M, Taeda K and Matsumoto N 1986 *Solid State Commun.* **57** 635
[3] Canham L T 1990 *Appl. Phys. Lett.* **57** 1046
[4] Takagi H, Ogawa H, Yamazaki Y, Ishizaki A and Nakagiri T 1990 *Appl. Phys. Lett.* **56** 2379
[5] Ziegler J F *TRIM-87 computer code* (IBM-Research, Yorktown Heights, NY 10598)
[6] Barbour J C, Dimos D, Guilinger T R, Kelly M J and Tsao S S 1991 *Appl. Phys. Lett.* **59** 2088

Distribution:

MS 0320	Org. 1102	Laura Lopez
MS 1056	Org. 1111	B. L. Doyle
MS 1056	Org. 1111	J. C. Barbour
MS 1056	Org. 1111	S. R. Lee
MS 1056	Org. 1111	D. A. Redman
MS 0350	Org. 1112	S. T. Picraux
MS 0350	Org. 1112	E. H. Chason
MS 1056	Org. 1112	D. M. Follstaedt
MS 0603	Org. 1322	T. E. Zipperian
MS 0603	Org. 1322	A. J. Howard
MS 1084	Org. 1323	R. V. Jones
MS 1084	Org. 1323	J. S. Custer
MS 1083	Org. 1332	P. S. Winokur
MS 1083	Org. 1332	J. W. Medernach
MS 0343	Org. 1822	J. A. Borders
MS 0343	Org. 1822	D. R. Tallant
MS 0342	Org. 1824	M. R. Keenan
MS 0342	Org. 1824	M. J. Kelly
MS 0609	Org. 1841	A. J. Hurd
MS 0609	Org. 1841	T. R. Guilinger (10)
MS 0609	Org. 1841	J. O. Stevenson
MS 0607	Org. 1845	P. F. Green
MS 0607	Org. 1845	D. B. Dimos
MS 0899	Org. 13414	Technical Library (5)
MS 0619	Org. 12613	Technical Publications
MS 0100	Org. 7613-2	Document Processing for DOE/OSTI (2)
MS 9018	Org. 8523-2	Central Technical Files